AN ABSTRACT OF THE DISSERTATION OF

Katrina Moran Hay for the degree of Doctor of Philosophy in Physics presented on April 29, 2008.

Title:

Physical Processes that Control Droplet Transport in Rock Fracture Systems

Abstract approved: _____

Maria I. Dragila

Aquifer recharge is generally driven by fluids that move from the Earths surface to groundwater through the unsaturated zone, also known as the vadose zone. When the vadose zone is fractured, fluids, which may include contaminants, can move through the fracture network as well as the porous matrix. Such a network of fractures can provide a more rapid path, thereby reducing contact time between the fluid and the matrix. Contact time allows for exchange of solutes between the fluid and the porous matrix, thus being able to quantify contact time is important. In addition, the behavior of fluids within a fracture network has been found to be very complex; large-scale models are yet not able to predict transport paths or flux rates. Because, small-scale flow phenomena can strongly influence the large-scale behavior of fluid movement through systems of fractures, it is important that small-scale dynamics be properly understood in order to

improve our predictive capabilities in these complex systems. Relevant flow dynamics includes the impact of boundary conditions, fluid modes that evolve in time and space and transitions between modes. This thesis presents three investigations aimed at understanding the physical processes governing fluid movement in unsaturated fractures, with the ultimate goal of improving predictive relationships for fluid transport in rock fracture systems. These investigations include a theoretical analysis of the wetting of a rough surface, an experimental study of the dynamics of fluid droplets (or liquid bridges) moving in a single fracture and a theoretical analysis of the movement of a fluid droplet encountering a fracture intersection. Each investigation is motivated by environmental applications. Development of an analytical equation for the wetting of a rough surface is based on a balance between capillary forces and frictional resistive forces. The resulting equation predicts movement of the liquid invasion front driven solely by the surface roughness; the relationship was found to exhibit a square root of time dependence. Rough surfaces also affect the movement of bulk fluid through the fractures. The speed of droplets moving downward between smooth and rough surfaces is seen to be significantly different. Experiments were used to develop predictive algorithms to calculate the speed of droplets in unsaturated rock fractures, which incorporate an adjusted contact angle for wet rough surfaces, and also incorporate the effect of dynamics on the evolution of the advancing contact angle. The third paper investigates the effect of intersection geometry on the larger scale distribution of fluid in a system of fractures. Fluid movement through fracture intersections depends on input flow

parameters, geometry of the system, and capillary and gravitational forces. The physical mechanisms governing the process are analyzed to predict distribution of liquid into fracture branches and velocity of the output flow. This study will improve the ability to incorporate pore-scale fluid physics phenomena into large-scale models for predicting flow transport in rock fracture systems.

Physical Processes that Control Droplet Transport in Rock Fracture Systems

by

Katrina Moran Hay

A DISSERTATION

submitted to

Oregon State University

in partial fulfillment of
the requirements for the
degree of

Doctor of Philosophy

Presented April 29, 2008
Commencement June 2008

Doctor of Philosophy dissertation of Katrina Moran Hay presented on April 29, 2008.

APPROVED:

Major Professor, representing Physics

Chair of the Department of Physics

Dean of the Graduate School

I understand that my dissertation will become part of the permanent collection of Oregon State University libraries. My signature below authorizes release of my dissertation to any reader upon request.

Katrina Moran Hay, Author

ACKNOWLEDGEMENTS

I would like to thank my research advisor, Dr. Maria Dragila for her patience, she has shared her passion for the research process with me and taught me to "find my question". I thank Dr. James Liburdy for his help in developing some of the theories presented here. The faculty and staff in the physics department have encouraged and supported me throughout my time in graduate school and I cannot thank them enough. Also, my Jet Propulsion Laboratory advisor, Dr. Carol Polanskey, helped me develop my professional skills and gave me an amazing internship opportunity. I acknowledge the NSF (Grant 0449928) for financial support.

TABLE OF CONTENTS

TABLE OF CONTENTS (Continued)

TABLE OF CONTENTS (Continued)

LIST OF FIGURES

LIST OF FIGURES (Continued)

LIST OF TABLES

DEDICATION

To Zach and my family, I would not have come this far without you.

Chapter 1 – Introduction

This chapter describes the motivation behind the research project described in this dissertation and the value of the results to the scientific community. It also covers general background material deemed necessary for the reader to understand the historical setting, and the implications of the research results herein. Three manuscripts in the form of chapters comprise the main body of the dissertation and follow the Introduction. The first manuscript has been submitted to the Journal of Colloid and Interface Science; the other two be submitted shortly.

How does fluid move from the surface to the ground water in dry rocky regions? What is the time frame of this process? In the case of contaminant or pesticide transport, how much fluid is left behind in the soil or rock matrix? Do the properties of the rock affect the way fluid moves along it? These are important questions that are not fully answered in the geologic and hydrologic communities. The study of fluid movement in large field systems is immensely complex, as well as difficult to observe and predict. The following manuscripts are presented to advance the understanding of small scale fluid physics as it pertains to rock fracture flow. The hope for this analysis is that it be used to aid in the modeling of fluid movement in larger fracture systems. There is still much to understand about the physics of fluid movement in fractures, however, simplified fluid physics investigations can enhance the predictive relationships in a way that does not require empirical formulas.

1.1 Applications of pore-scale fluid physics

Fluid flow physics spans many disciplines in science, explaining microbiological transport, colloid movement, arterial blood flow, rain on windshields, geologic erosion, ocean and atmospheric circulation, sand dune migration and galaxy collisions all using generally the same basic principles. Many processes in the universe, though governed by different mechanisms, are underlain by similar simple physical concepts. Forces acting on a fluid may be few in number, yet the resulting behavior can still be extremely complicated, often nonlinear. For this reason, computers are often employed to simulate fluid movement. However, questions remain that may be answered simply with conceptual investigations of small-scale fluid physics; it is small scale fluid movement that controls behavior of fluid movement at large scales. The focus of this dissertation is to expose some of these small-scale phenomena and provide tools for improved modeling of systems that involve both large and small scale fluid movement in the context of rough-walled fracture networks.

1.1.1 Environmental applications

An important application of this work is liquid contaminant transport in unsaturated rock fractures. Some dry rocky regions of the United States have subsurface features that include narrow rock fractures that intersect each other; this network can extend down to the ground water. The clean up effort at Hanford nuclear facility and Idaho National Labs, and the characterization of the Yucca Mountain nuclear repository are major efforts for whom this research is relevant. Over the

past two decades significant scientific resources have been dedicated towards better estimates of solute transport through fractured vadose zones, with a goal of predicting the speed and other properties of fluid movement in areas such as these (Browning et al., 2003; Pruess et al., 2002). In fractured porous media, fractures can serve as preferential pathways for flow (Su et al., 2003), effectively acting as short circuits to what is otherwise a porous media transport process. It has been observed that in two phase flow, such as water and air, small scale behavior can impose significant controls on large scale fluid behavior. Laboratory experiments that study the dynamics of fluid through fractures can provide valuable insight to improve numerical modeling efforts (Dragila and Weisbrod, 2003; Glass et al., 2002; Wood et al., 2004; Fairley et al., 2004; Su et al., 2001; Su et al., 2003; Su et al., 2004).

The agricultural community is also concerned with fluid movement in the vadose zone (the zone spanning from the surface to the ground water). The vertical and lateral movement of pesticides is a complicated problem and requires an understanding of fluid interaction with various subsurface properties and processes. Fluid movement in macropores is becoming increasingly important as soil physicists look at the importance of preferential flow pathways in the subsurface (Su, et al., 2003; Nimmo et al., 2007) and its effect on nutrient availability to crops and on movement of plant nutrients to aquifers. In addition, the transfer of a dissolved substance between a porous rock and a moving fluid within a fracture depends on the porosity of the rock, the roughness of the surface, and the dynamics of the fluid.

1.1.2 Engineering applications

The applications of pore-scale fluid physics are not limited to environmental studies. The question of surface wettability is important in many industrial engineering fields as well. Research focused on wetability of surfaces is used to improve manufacturing of hydrophobic and hydrophilic surfaces. Wetability or water-repellancy of natural and artificial porous surfaces is investigated with applications such as rain-resistant clothing and the spreading rate of ink. For example, water resistance of a duck's feathers is due to the structure of the feathers rather than any exceptional proofing agent (Cassie and Baxter, 1944). The process of wetting a surface by a fluid is governed by the interfacial forces. In addition, the geometry of the surface can result in the development of curved interfaces creating capillary forces that are able to enhance or reduce wettability. Using purely interfacial energy, the coating fluid may also be removed by another fluid with greater wetting properties (Bico and Qu*éré*, 2002).

The effect of surface roughness on wettability is of interest in other industrial applications. Some applications take advantage of the ability of a rough surface to maintain a wetted layer. For example, the contact lens industry must create lenses that are rough enough to maintain a wet layer, yet smooth enough to be comfortable for the wearer.

1.2 Recent relevant work

1.2.1 Flow modes in fractures

It is one matter to study the flow dynamics of a saturated (fluid-filled) parallel plate geometry, it is completely another to consider both liquid and gas occupying the space between parallel plates. This added level of complexity greatly affects the flow behavior because a multiphase system contains interfaces between liquid and gas, which give rise to strong interfacial forces. On a laboratory scale, these interfacial surface forces become important in controlling the motion of fluid and gas. Multiphase flow in fractured rock can exhibit several different forms, each having different properties that greatly impact overall transport and interaction with the solid substrate. Major classifications of flow modes in parallel rough plates include droplets, rivulets, streamlets and films (Su et al., 2004). A droplet is a suspended liquid bridge between parallel plates; a rivulet is also suspended but resembles a string as opposed to a blob of fluid; streamlets are defined as rivulets with one liquid-solid contact and one free surface; films are in contact with only one of the parallel plates and have non-negligable width. Experimental investigations show that geometric and fluid properties influence the mode of flow (Su, 1999). Experiments also show that even the scale of roughness can influence the mode of flow that dominates a given system, for example the scale of roughness is important in determining whether or not a droplet or rivulet will form (Su et al., 2004).

Flow mode affects speeds, extent of exposure and time of exposure to the solid.

For example, a continuous rivulet flow can allow rapid solute transport but maintain a relatively small contact area with the fracture wall (Dragila and Weisbrod, 2004). Understanding the small-scale mechanisms controlling flow properties like speed and mode of transport is important for developing conceptual models describing seepage, absorption and distribution of liquids in unsaturated, fractured media. Detailed theoretical analysis will help to characterize the flow modes and possible flow behaviors.

1.2.2 Droplets

Of the flow modes descibed in the previous section, this project focuses on the behavior of droplets. Much work has been done to create a complete mathematical description of a pendant droplet (Ghezzehei and Or, 2005) and of droplets in motion between parallel plates. A droplet that wets the surface leaves a film behind on either plate, decreasing the volume of the droplet as it moves and making the receding contact angle zero (Bico and Qu*éré*, 2001). A droplet can move due to gravitational forces or thermal and chemical gradients. In the case of a droplet moving by gravity, the curvatures of the advancing and receding menisci of the droplet provide additional surface forces that usually slow the droplet's speed.

Droplets can form as a film encounters a local reduction in the fracture aperture. The detachment of a droplet from a supply of fluid in this case depends on capillary forces, aperture and liquid weight (Ghezzehei and Or, 2005); the volume of the droplet that is released from the constriction is then a function of the fracture

aperture.

With Navier-Stokes-based theoretical models, the speeds of droplets between smooth glass plates has been adequately described (Dragila and Weisbrod, 2003). Dragila and Weisbrod not only account for the curvature of the advancing and receding edge of the droplet, they also allow for a dynamic advancing contact angle. However, surface roughness provides an added challenge and has not been fully understood or quantified in the context of the droplet flow mode. The equation of Dragila and Weisbrod (2003) significantly underpredicts the speed of droplets on rough and porous surfaces.

1.2.3 Rough and porous fractures

Glass is commonly used to model rock when experimentally simulating rock fracture flow because it provides a hard surface for the fluid to move on and the transparency makes for convenient laboratory studies. However, fluid behaves differently on rough surfaces than on smooth surfaces. Roughness can affect the determination of flow form in a fracture. Water becomes trapped in roughness, forming a film on the surface after drainage of a droplet through a fracture (Su et al., 2004).

Droplets on tile (porous) surfaces have faster speeds than droplets on smooth glass plates (Steele, 2004). This suggests that solute transport in rock fractures may be significantly higher in real rock systems than in smooth glass simulated ones. In order to adequately model rock fracture flow, transport theories should

allow for rock surfaces to be rough and porous. While texture of rock can be simulated to some degree by sand blasting the glass surface, porosity cannot be simulated.

1.2.4 Fracture systems and intersections

Experiments suggest that a porous fracture network can give rise to preferential flow paths, but paths can change over time. When a supply of water was applied to the top of an uncemented wall composed of porous bricks, dynamic preferential pathways were observed (Glass et al., 2002). In a similar experiment, where a constant water supply was introduced to a thin wall of uncemented limestone blocks, preferential flow paths were observed and flow tended to converge to a single fracture at the bottom layer of blocks (Wood et al., 2004). Preferential pathways could also switch gradually or abruptly and periods of pathway switching was more common than periods of steady flow. In this experiment, intersections served as capillary barriers and locations where fluid would accumulate until a critical amount was reached then fluid would proceed, generating less frequent larger pulses of water (Wood et al. 2002) . Wood et al. also found that even under similar laboratory conditions, the advancing wetting front was not repeatable in multiple experiments. Common modeling approaches cannot yet duplicate this nonideal, dynamic flow through a fracture network. Porous systems such as these seem to be highly sensitive and unreproducible either in other experiments and theoretical models. While both roughness and porosity may affect the boundary

conditions of flow though fractures, it is necessary to separate the two concepts and deal with them as being responsible for different physical mechanisms.

At the scale of a single fracture intersection, Dragila and Weisbrod (2004) performed experiments to study the evolution of a fluid droplet as it moved down a fracture and across a symmetric three-way intersection. A curved fluid interface creates a capillary force towards the inside of the curvature; the smaller the curvature, the stronger the force. As a droplet advances into an intersection, the aperture widens allowing the advancing curvature to become greater, while the receding end experiences the same upward capillary force as it did prior to intersection arrival. In some cases, this change can be great enough to keep the droplet from penetrating into the intersection, the weight of the droplet cannot overcome the net capillary force upward. This phenomenon is called a capillary barrier. The intersection can serve as a capillary barrier, holding fluid behind it until a critical mass (gravitational component) can overcome the capillary barrier. Other observations included the transition of a droplet to two films or to a droplet and a film at the intersection, as well as a droplet which entered one of the intersection branches then rebounded, moving into the alternate branch.

Some numerical modeling approaches such as the method of volume of fluid (VOF) (Huang et al., 2005) and smoothed particle hydrodynamics (SPH) (Tartakovsky, 2005) have successfully modeled intersection dynamics and reproduced experimental results. However, further simplified analytical formulas are needed. Computational modeling is useful in visualizing pore-scale fluid movement, but these models are not necessarily simple or inexpensive to upscale to large networks

of fractures. To upscale, you still need to know the effects of fluid interaction with the fracture boundaries and intersections. For these reasons, some simple analytical rules (equations) would be powerful in predicting and testing various scenarios of intersection geometries and systems of intersections.

1.3 Challenges: Pore-scale physics phenomena

1.3.1 Surface effects and the contact angle

Pore-scale refers to the scale at which surface forces are as dominant as gravity. Surface tension is the force against which you are doing work when you stretch a surface. A fluid-air interface can be thought of as a rubber membrane, acting to reduce the surface area.

When surface tension is expressed over a curved surface, an important effect arises called capillarity. Capillarity is the phenomenon by which a water wicks up a capillary tube, a small glass tube that is put in contact with a wetting fluid, such as water. The curved surface is created by the competition of two forces, the cohesive forces between water molecules that act to reduce the interfacial surface area to lower its surface energy, and adhesive forces between the glass and the water that tend to spread the water along the glass tube. The result is a concave shape that generates a force towards the inside of the curvature. In the case of mercury, for example, where cohesive forces are stronger than adhesive forces, the curvature is convex, and the liquid height in the tube is depressed. The capillary

force commonly exceeds the force of gravity on small scales. As an example of this force, the air inside of a bubble has increased pressure compared to the air outside the bubble due to the force toward the inside of the curvature.

A curved interface can be described by the two principal radii of curvature of any two orthogonal planes intersecting normal to the surface, R_1 and R_2. The difference in pressure, ΔP, across this interface is described by the Young-Laplace Equation,

$$\Delta P = \gamma\Big(\frac{1}{R_1} + \frac{1}{R_2}\Big), \tag{1.1}$$

where γ is the surface tension (Butt, 2006).

A drop of fluid placed on a solid surface forms an interface with a shape governed by the properties of the fluid, the solid and gas or other fluid (usually air). A balance of the surface tensions between liquid-gas, liquid-solid and solid-gas give rise to a contact angle, which defines a static equilibrium of these forces (see free-body diagram in Fig. 1.1). Young's Equation relates the contact angle to the interfacial tensions,

$$\gamma_{LG}\cos\theta = \gamma_{SG} - \gamma_{SL}, \tag{1.2}$$

where θ is the contact angle (inside the liquid drop) and the subscripts of the surface tension represent interactions between two of the three phases, liquid (L), gas (G) or solid (S) (Butt, 2006). This force balance is for the horizontal direction in Fig. 1.1, and it is interesting to note that there remains a vertical component of the liquid-gas surface tension that is unbalanced. This left over force is why a water droplet on fresh paint, once dry, will leave a slight peak around the perimeter

of the droplet. Fluids with contact angles that are less than 90° are said to be wetting or having a hydrophylic interaction with the solid surface; contact angles greater than 90° correspond to non-wetting or hydrophobic interactions.

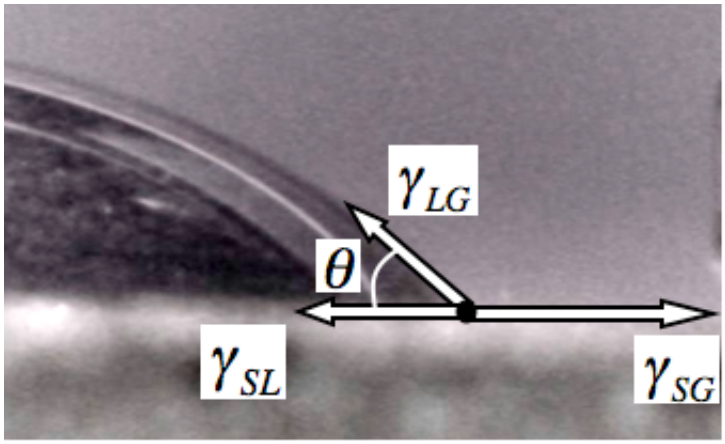

Figure 1.1: Surface tensions between liquid, gas and solid govern the value of the contact angle.

1.3.2 Contact line dynamics

The previous section discussed issues associated with static conditions. A moving contact line can be extremely complex and the topic of contact line dynamics has a history rich in controversy. The assumption that a moving fluid that is in contact with a solid must have a zero velocity at the location immediately adjacent to the solid, leads to the idea that droplets move by rolling. This rolling motion has been observed experimentally (Dussan, 1974). It has been suggested that fluid moving along a solid surface will exhibit a rolling motion at least at the location of the

three-phase contact line. However, this implies that all contact angles be 180°, if the macroscopic contact angle is governed by the microscopic contact angle. Since it has been observed that not all fluids are this hydrophobic, there must be a different explanation. Conceptually allowing the rolling motion to occur while forcing the interface to sustain the shape governed by the known contact angle leads to a serious mathematical problem (a singularity), which occurs right at the point of the three -phase intersection. Consider an advancing fluid interface across a solid surface. As the fluid rolls, a particle from the outermost liquid adjacent to the gas passes through the point where all three phases meet and becomes a fluid particle that is no longer in motion because it is adjacent to the solid boundary. By definition, the fluid adjacent to a solid cannot move (no-slip boundary condition). The motion of the fluid as it goes from moving to not moving abruptly is not allowed and results in a singularity.

There are many hypothesis for the relief of this mathematical singularity at the three-phase contact line. One popular way of avoiding the singularity is to allow for a slip condition in the region of the contact line (Huh and Mason, 1977; Thompson, 1989). It turns out that reasonable slip lengths are at the atomic scale (Dussan, 1991).

Another way to account for the singularity is to assume that the physical mechanisms controlling motion are different at different scales in the problem (De Gennes, 1990). At a molecular level, a surface or interface is not a sharp boundary. Fluid molecules are attracted to each other and as a fluid boundary moves across a solid, the molecules bounce around and become attracted to the solid, eventually the fluid

molecules slow down when they are next to the solid and the delay in this action allows for no particle to experience a singularity in it's velocity. It is also known that a precursor film of molecular thickness advances ahead of a macroscopic drop and is driven by molecular forces (Nieminen, 1992). Fortunately, the singularity and precursor film are only relevant at the micro-level and can be ignored when looking at mesoscale and macroscale problems.

A dynamic phenomenon that does concern the pore-scale is a dynamic contact angle. A moving contact angle increases as a function of the speed of the advancing interface (Hoffman 1974, Hofman 1983).

1.4 Roughness

There are many phenomena in fluidics related to roughness. Roughness can change the contact angles between fluid and solid and enhance hydrophobicity or hydrophilicity (Wenzel, 1936; Bico et al., 1999). A rough surface can maintain a wet layer longer than a smooth surface. It wicks a wetting fluid like a sponge (Bico and Qu*é*r*é*, 2001; Cazabat et al., 1986). Since rock surfaces exhibit roughness, studying roughness will help us understand contact line dynamics in rock fracture flow. Experiments show that the scale of roughness can influence the mode of flow that dominates a given system (Su et al., 2004). In the context of droplet flow mode, surface roughness provides an added challenge and has not been fully understood or quantified.

1.5 Introduction to subsequent chapters

The three chapters that follow discuss conceptual and experimental investigations that elucidate some of the physical mechanisms controlling fluid movement in rock fracture systems.

The focus of the first manuscript is to understand how texture affects fluid movement. A wetting fluid spreads further and faster on a rough surface than on a smooth surface (see Fig. 1.2). The premise of the theory presented involves the role of the capillary force at the scale of surface roughness. While it is important to understand this mechanism for both wetting interaction and non-wetting interactions, the theory presented proposes the physical mechanism responsible for the wetting of a rough surface, and is only valid for a wetting interaction.

The second manuscript focuses on the droplet flow mode, making an addition to the current theoretical description for the motion of droplet in the case of rough surfaces. A suggestion is made for further investigation regarding the internal flow dynamics of moving droplets.

In fracture networks, small scale fluid physics can significantly affect large scale fluid behavior. Consider when a droplet of fluid approaches an intersection of fractures; how much of the fluid will go into each branch? The third manuscript provides an analytical formula for calculating the volume ratio of the distribution of liquid when a droplet encounters an intersection. The equation is also used to investigate the limits of larger scale dispersion of a fluid plume in a fracture network system. Some examples are given of how these intersection rules may be

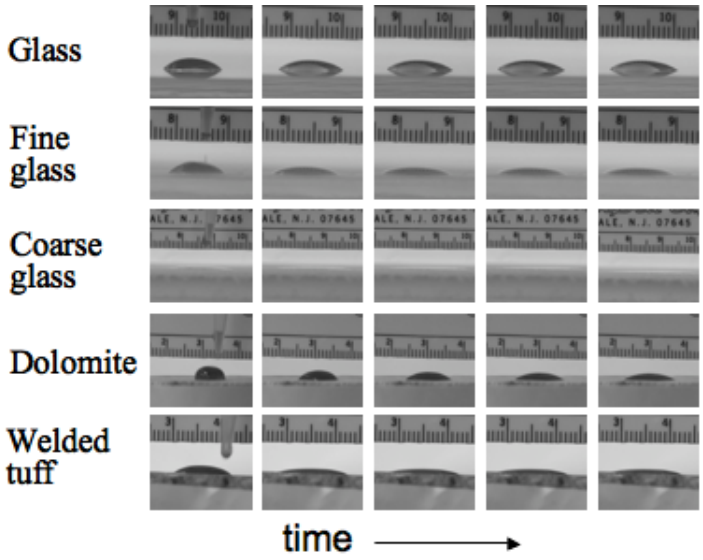

Figure 1.2: Water droplet progressions on a smooth glass surface and on various types of roughness: fine and coarsely sandblasted glass and two types of rock, dolomite and welded tuff. The images advance in time to the right and increase by one second for each image.

used to upscale to multiple intersections. The goal of intersection modeling is to be able to predict from initial conditions (i.e. how much fluid, what type of fluid) the motion (i.e. how far the fluid will move vertically downward and laterally, how fast the fluid will do this). Accomplishing this would be of significant use to geologic and agricultural communities interested in contaminant flow through fractured media.

1.6 References

Bico, J., Marzolin, C., Qu*é*ré, D., 1999. Pearl drops. Europhysics Letters 47(2): 220-226.

Bico, J., Qu*é*ré, D., 2001. Falling Slugs. Journal of Colloid and Interface Science 243:262-264.

Bico, J., Qu*é*ré, D., 2002. Self Propelling Slugs. Journal of Fluid Mechanics. 467:101-127.

Bico, J., Tordeux, C., Qu*é*ré, D., 2001. Rough Wetting, Europhysics Letters, 55: 214-220.

Browning, L., Murphy, W.M., Manepallya, C., Fedorsa, R., 2003. Reactive transport model for the ambient unsaturated hydrogeochemical system at Yucca Mountain, Nevada. Computers & Geosciences 29 (3): 247-263.

Butt, H-J., Graf, K., Kappl, M., 2006. Physics and Chemistry of Interfaces. Wiley-Vhc Verlag Gmbh & Co. KGaA, Weinheim

Cassie, A.B.D., Baxter, S., 1944. Wetability of porous surfaces. Transactions of the Faraday Society Articles 40: 546 - 551

Cazabat, A.M., Cohen Stuart, M.A., 1986. Dynamics of Wetting: Effects of Surface Roughness, Journal of Physical Chemistry, 90: 5845-5849.

De Gennes, P.G., Hua, X., Levinson, P., 1990. Dynamics of wetting: local contact angles. Journal of fluid mechanics 212:55-63.

Dragila, M.I., Weisbrod, N., 2003. Parameters affecting maximum fluid transport in large aperture fractures. Advances in Water Resources 26: 1219-1228.

Dragila, M.I., Weisbrod, N., 2004. Flow menisci corners of capillary rivulets. Vadose Zone Journal 3: 1439-1442.

Dragila, M.I., Weisbrod, N., 2004. Fluid Motion through an unsaturated fracture junction. Water Resources Research. 40: W02403.

Dussan, E.B., Davis, S.H., On the motion of a fluid-fluidinterface along a solid surface. Journal of Fluid Mechanics 65(1): 71-95.

Dussan, E.B., Rame, E., Garoff, S., 1991. On identifying the appropriate boundary conditions at a moving contact line: an experimental investigation. Journal of Fluid Mechanics 230:97-116.

Fairley, J.P., Podgorney, R.K., Wood, T.R., 2004. Unsaturated flow through a small fracture-matrix network: Part 1. Uncertainty in modeling flow processes. Vadose Zone Journal 3:101-108.

Glass, R.J., Nicholl, M.J., Pringle, S.E., Wood, T.R., 2002. Unsaturated flow through a fracture-matrix network: Dynamic preferential pathways in mesoscale laboratory experiments. Water Resources Research 38(12): 1281-1298.

Hoffman, R.L., 1974. A study of the advancing interface I. Interface shape in liquid-gas systems. Journal of Colloid and Interface Science 50(2): 228-241.

Hoffman, R.L., 1983. A study of the advancing interface I. Theoretical prediction

of the dynamic contact angle in liquid-gas systems. Journal of Colloid and Interface Science 94(2): 470-486.

Huang, H., Meakin, P., Liu, M., 2005. Computer simulation of twophase fluid motion in unsaturated complex fractures using volume of fluid method. Water Resources Research 41: W12413.

Huh, C., Mason, S.G., 1977. The steady movement of a liquid meniscus in a capillary tube. Journal of Fluid Mechanics 81(3): 401-419.

Nieminen, J.A., Abraham, D.B., Karttunen, M., Kashi, K., 1992. Molecular dynamics of a microscopic droplet on solid surface. Physical Review Letters 69(1): 124-127.

Nimmo, J.R., 2007. Simple predictions of maximum transport rate in unsaturated soil and rock. Water Resources Research. 43, W05426.

Pruess, K., Yabusakib, S., Steefelc, C., Lichtnerd, P., 2002. Fluid Flow, Heat Transfer, and Solute Transport at Nuclear Waste Storage Tanks in the Hanford Vadose Zone. Vadose Zone Journal, 1:68-88

Steele, B., 2004. A Comparison of Theoretical and Experimental Capillary Droplet Speeds on Porous and Non-Porous Fracture Surfaces. Master of Environmental Soil Science Thesis, Oregon State University, Corvallis, Oregon.

Su, G.W., 1999. Flow Dynamics and Solute in Unsaturated Rock Fractures. PhD Thesis, University of California Berkley, Department of Civil and Environmental

Engineering and Ernest Orlando Lawrence Berkley National Laboratory, Earth Sciences Division.

Su, G.W., Geller, J. T., Hunt, J.R., Pruess, K., 2004. Small-scale features of gravity-driven flow in unsaturated fractures. Vadose Zone Journal 3:592-601.

Su, G.W., Geller, J.T., Pruess, K., Hunt, J.R., 2001. Solute transport along preferential paths in unsaturated fractures. Water Rsources Research 37(10): 2481-2491.

Su, G.W., Nimmo, J.R., Dragila, M.I., 2003. Effect of isolated fractures on accelerated flow in unsaturated porous rock. Water Resources Research 39(12):1326-1335.

Tartakovsky, A.M., Meakin, P., 2005. Simulation of unsaturated flow in complex fractures using smoothed particle hydrodynamics. Vadose Zone Journal 4:848-855.

Thompson, P.A., Robbins, M.O., 1989. Simulations of contact line motion:slip and the dynamic contact angle. Physical Review Letters 63(7): 766-769.

Wenzel, R.N., 1936. Resistance of Solid Surfaces to Wetting by Water. Industrial Engineering Chemistry, 28: 988-994.

Wood, T.R., Glass, R.J., McJunkin, T.R., Podgorney, R.K., Laviolette, R.A., Noah, K.S., Stoner, D.L., Starr, R.C., Baker, K., 2004. Unsaturated flow through a small fracture-matrix network: Part 1. Experimental Observations. Vadose Zone

Journal 3:90-100.

Wood, T.R., Nicholl, M.J., Glass, R.J., 2002. Fracture intersections as integrators for saturated flow. Geophysical research letters, 29(24): 2191

Chapter 2 – A Theoretical Model for the Wetting of a Rough Surface

K.M. Hay[1], M.I. Dragila[2] , J. Liburdy[3]

[1]Department of Physics, Oregon State University, Corvallis, Oregon

[2]Department of Crop and Soil Sciences, Oregon State University, Corvallis, Oregon

[3]Department of Mechanical Engineering, Oregon State University, Corvallis, Oregon

Reproduced from submission:

Journal of Colloid and Interface Science

Elsevier Publishing

February 14, 2008

2.1 Abstract

Many applications would benefit from an understanding of the physical mechanism behind fluid movement on rough surfaces, including the movement of water or contaminants within an unsaturated rock fracture. Presented is a theoretical investigation of the effect of surface roughness on fluid spreading. It is known that surface roughness enhances the effects of hydrophobic or hydrophilic behavior, as well as allowing for faster spreading of a hydrophilic fluid. A model is presented based on the classification of the regimes of spreading that occur when fluid encounters a rough surface: microscopic precursor film, mesoscopic invasion of roughness and macroscopic reaction to external forces. A theoretical relationship is developed for the physical mechanisms that drive mesoscopic invasion, which is used to guide a discussion of the implications of the theory on spreading conditions. Development of the analytical equation is based on a balance between capillary forces and frictional resistive forces. Chemical heterogeneity is ignored. The effect of various methods for estimating viscous dissipation is compared to available data from fluid rise on roughness experiments. Methods that account more accurately for roughness shape better explain the data as they account for more surface friction; the best fit was found for a hydraulic diameter approximation. The analytical solution implies the existence of a critical contact angle that is a function of roughness geometry, below which fluid will spread and above which fluid will resist spreading. The resulting equation predicts movement of a liquid invasion front with a square root of time dependence, mathematically resembling

a diffusive process.

2.2 Keyword

roughness, wetting, capillarity

PACS 47.15.G-

2.3 Introduction

This manuscript poses a conceptual model and theoretical construct for the physical mechanism driving fluid spreading into a rough surface. Currently, surface design used to manipulate wetting properties depends on empirical theories pertaining to wetting of rough surfaces. There are few publications aimed at describing the physical mechanism governing this phenomena (Bico et al., 2001; Cazabat et al., 1986). What drives a fluid to invade texture? What factors resist this movement? These questions must be answered in order to describe the process of fluid invasion into roughness. In order to understand the importance of the assumptions made in the development of the theoretical model presented here, it is necessary to give a brief history of the exploration of roughness and its effect on fluid movement.

Wenzel (Wenzel, 1936) may have been the first person to analyze the effect of surface roughness on the static contact angle (the angle subtended at the triple-phase line formed by a fluid-air-solid interface). He observed that surface roughness caused a hydrophobic fluid to behave as if it were more hydrophobic and a

hydrophilic fluid to behave as if it were more hydrophilic. Wenzel also suggested that the geometry of the surface had a greater effect on the static contact angle than did the chemistry.

Bico *et al.* (2001) suggest that a surface's geometry can be used to tune it's wetting properties. From experimental observations, they derive a diffusion law for fluid spreading based on the change in energy that accompanies movement of the contact line. Their work focused on the behavior of the gas-liquid-solid interface for a hydrophilic fluid on a rough surface. Their diffusion law contains a parameter, β that is an experimentally measured property of each rough surface and accounts for the increase in viscous forces caused by the presence of rough spikes. Bico's introduction of this important concept of capillarity is essential to the analysis presented here.

Cazabat and Cohen Stuart (1986) explored the effects of surface roughness experimentally. They observed hydrophilic fluid drops spreading on smooth and rough surfaces and recorded the radial size of the drop as a function of time. Drops on rough surfaces behaved differently than on smooth surfaces. It was observed that the spreading rate on rough surfaces followed two distinct power laws. The mechanisms for these two spreading regimes were suggested to be a capillarity-dominated behavior followed by a gravity-dominated behavior. Initially, the macroscopic cap of the drop sustains a gravity-dominated shape, while some of the fluid spreads from the macroscopic edge, *into* the roughness. Eventually fluid in the macroscopic drop relaxes onto the fluid that had invaded the roughness. They hypothesized that the initial invasion process is the result of an "essentially

constant capillary force" pulling the fluid into the surface roughness. The functional dependence of the spreading distance on the square root of time suggests that the process is described by a diffusion law; the functional dependence on time and diffusion coefficients for various rough surfaces were found experimentally.

The effect of roughness on hydrophobicity has been examined by Quere (2002). Quere, starting from Wenzel's ideas, described the energy change due to the movement of a contact line on a rough surface, thereby deriving Wenzel's equation from an energy standpoint. The investigation presented here focuses on hydrophilic interactions where a liquid front is expected to advance over a rough surface rather than recede.

It is the goal of this study to derive an analytical model for the invasion process and develop an equation for the speed of the invasion front, that depends solely on the properties of the fluid and the solid. The model incorporates the geometry of the surface roughness to generate the capillary driving force suggested by Bico and Cazabat as well as competing resistive viscous forces; accuracy is sensitive to the specification of surface geometry. An idealized theoretical rough surface model is used that coincides with the micropatterned surface used by Bico *et al.* (2001) (Fig. 2.1) to permit comparison of the theoretical model to experimental results. The physical mechanism suggested in this model may mathematically correspond to the empirical coefficient of proportionality, β, in Bico *et al.*'s diffusion model. The goal of the mathematical model is to predict the wetting behavior on a surface, given the basic surface structure.

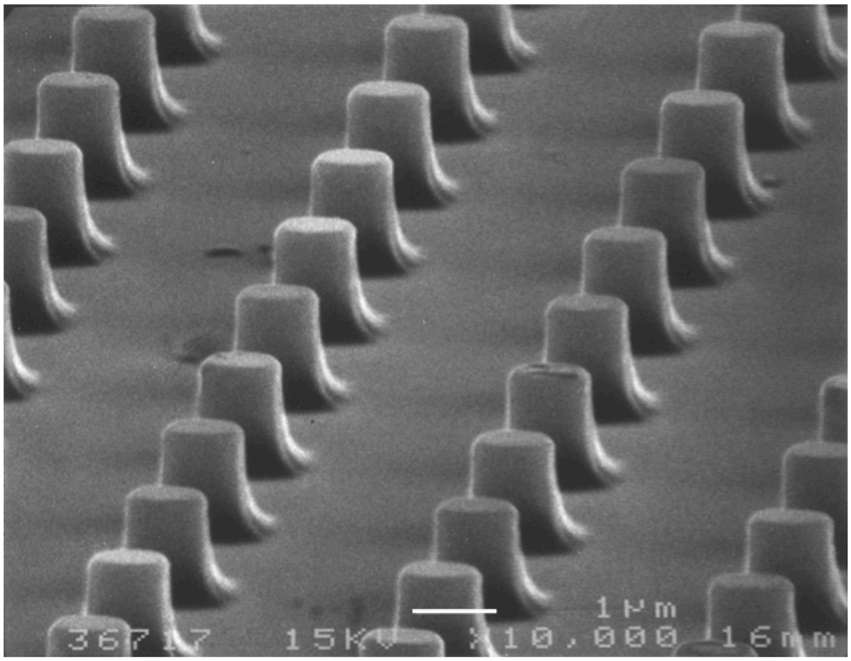

Figure 2.1: Microstructure with regular micronic cylindrical spikes used for the experiment of Bico *et al.* 2001.

2.4 Theory

Let us define three regimes of spreading: precursor film, roughness invasion and reaction to external forces (Fig. 2.2). It is known that a microscopic *precursor film* precedes the contact line of a fluid that is in contact with a solid. Movement of the precursor film is governed by molecular diffusive transport of vacancies from the tip of the film to the edge of the macroscopic meniscus (Burlatsky et al., 1996). It is assumed here that the precursor film must also occur on rough surfaces and this will be considered the first regime of spreading. The second regime of spreading on a rough surface is the gravity-independent mesoscopic fluid invasion into the

rough texture driven by capillary forces and will be the focus of this manuscript. The third regime begins when the macroscopic meniscus relaxes into its new shape or location governed by external forces, such as gravity.

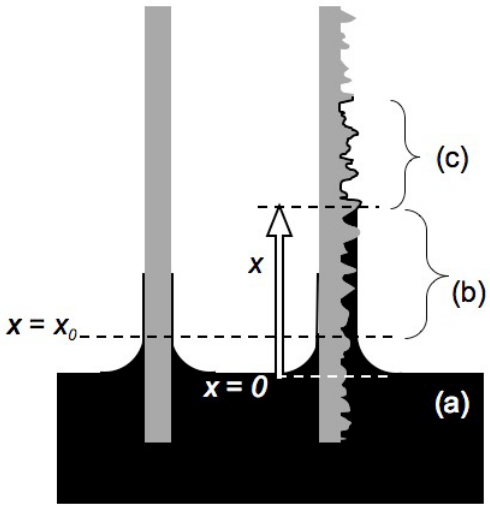

Figure 2.2: Fluid (black) rise on solids (grey), not to scale; Both smooth surface (left) and rough surface (right) show a meniscus to the height of x_0. Rough surface regimes: a) bulk fluid; b) mesoscopic fluid invasion regime (fills in the roughness); c) precursor film (on the order of 100 Angstroms thick) shown on both illustrations. x is measured from the bulk fluid to the edge of the invasion regime.

The geometric model for surface roughness is here idealized as comprised of a series of small cylindrical elements arranged on an otherwise smooth surface. This idealization is used to simplify the forces acting on the fluid and is a convenient choice as experimental data from Bico *et al.* (2001) describes spreading on a similar micropatterned surface (Fig. 2.1). The model assumes that invasion into the rough surface is driven solely by capillary forces; gravity is ignored for this regime (Bico et al., 2001; Cazabat et al. 1986). Other simplifiing assumptions

made are that the system is isothermal, the solid, liquid and vapor elements are chemically homogeneous and there is no evaporation. Chemical heterogeneity is ignored as a driving mechanism.

The next sections calculate the driving and resisting forces and then combine them, resulting in an equation for the invasion speed. Flow is governed by the Navier-Stokes momentum-conservation equation

$$\rho(\vec{u} \cdot \nabla)\vec{u} = \rho\vec{g} - \nabla P + \mu\nabla^2\vec{u}, \tag{2.1}$$

where ρ is the fluid density, $\vec{u}$ is the velocity vector, $\vec{g}$ is the acceleration due to gravity, P is the pressure, and μ is the dynamic viscosity. These equations can be reduced with some simplifying assumptions for the case of fluid movement over a surface. Gravity is ignored, even for vertical roughness invasion; experimental investigations suggest that roughness invasion is driven by strong capillary forces and the effect of gravity on the motion of the invasion fluid is negligible (Bico et al., 2001; Cazabat et al. 1986). The resulting invasion fluid velocity, U, is proportional to the pressure gradient across the invading fluid, ∇P, where ∇P is a result of capillarity created by the curvature of the advancing fluid-air interface. The proportionality is dependent on the geometry of the surface because different shapes will have different viscous effects. Eq. 4.2 is reduced for the case of film flow driven by a pressure gradient to be

$$\mu\frac{\partial^2}{\partial y^2}u = \frac{dP}{dx}, \tag{2.2}$$

where the y-direction is perpendicular to the surface and u is the velocity in the direction of motion (x in Fig. 2.2). For flow in a pipe, the relevant equation for pressure-driven flow is

$$\frac{\mu}{r}\frac{\partial}{\partial r}\Big(r\frac{\partial}{\partial r}u\Big) = \frac{dP}{dx}, \tag{2.3}$$

where, r is the cylindrical radial component and u is the velocity in the direction of flow in the pipe (x).

The next sections discuss several approximations for the shape of the surface which lead to invasion solutions of the form $x \propto t^{1/2}$, where x is the distance traveled by the invasion front and t is the time it takes to travel that distance, and where frictional effects, and therefore the geometry of the rough surface govern the proportionality constant. The effect on viscous dissipation of various models used to represent the geometry of the rough surface are investigated; first a hydraulic diameter approximation which allows for a more specific characterization of the surface roughness is presented and then simpler, though less accurate, methods are discussed. All methods discussed are based on representing the rough surface as a series of parallel channels. Following the approach of Washburn (1921), for calculating imbibition rates in porous media, the method presented here assumes that capillarity is the driving force. However, while Washburn assumed pores could be modeled as tubes, surface roughness can pose a more complex geometry. In fact, as shown later, assuming half-pipe channels is insufficient to account for the resistive forces on the fluid.

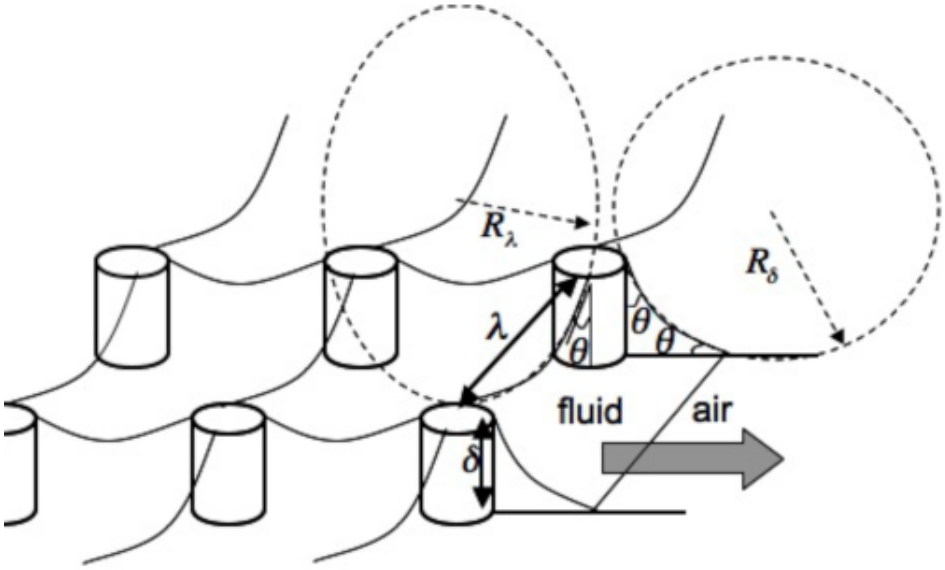

Figure 2.3: Illustration of the fluid-air interface created by the presence of roughness. All gas-fluid-solid contact angles (θ) are identical. Interface curvature creates capillarity and drives flow. Fluid movement is in the direction of the shaded arrow. Determination of the radius of curvature is governed by λ and δ.

2.4.1 Capillary driving mechanism

The curvature of the front edge of the spreading liquid will decrease the liquid pressure along the front, creating a pressure gradient between the main liquid resevoir and the invasion front. It is this pressure gradient that drives the invasion process. The capillary pressure is described by the Young-Laplace equation,

$$\Delta P_c = \gamma\Big(\frac{1}{R_\delta} + \frac{1}{R_\lambda}\Big) \tag{2.4}$$

where ΔP_c is the pressure difference across the liquid-air interface caused by capillarity, γ is the liquid-gas surface tension, and R_δ and R_λ are the radii of curvature (δ denotes the height of the cylinders and λ is the distance between cylinder edges, not center to center) as shown in Fig. 2.3. If the modeled roughness elements (i.e. cylinders) are normal to the smooth surface, and θ is the gas-liquid-solid contact angle determined by the surface energies, then

$$R_\delta = \frac{\delta}{\cos\theta - \sin\theta} \tag{2.5}$$

$$R_\lambda = \frac{\lambda}{2\cos\theta} \tag{2.6}$$

Substituting Equations 2.5 and 2.6 into Equation 2.4 and assuming the pressure in the bulk macroscopic fluid equals the external pressure, then which means the change in pressure across the liquid-gas interface is equal to the pressure difference between the invasion front and the macroscopic fluid edge. The force per unit area driving the fluid into the rough texture is

$$\Delta P_c = \gamma\Big(\frac{(2\delta + \lambda)\cos\theta - \lambda\sin\theta}{\delta\lambda}\Big). \tag{2.7}$$

2.5 Frictional resistive mechanism using hydraulic diameter approximation

In this section, we calculate the pressure loss due to viscous dissipation during fluid motion, the left-hand side of equation 2.2, or 2.3. For this derivation, the surface geometry shown in Fig. 2.3 is further simplified as a series of parallel channels of depth δ and width λ. A hydraulic diameter formulation is used to approximate the complex geometry of the rough surface (the no-slip boundary) that is in contact with the moving fluid. The hydraulic diameter method approximates a non-circular flow duct (in this case an open rectangular channel) by introducing a length scale proportional to the ratio of the cross sectional area of flow to the wetted perimeter. This provides a measure of flow per frictional area.

The loss of pressure per unit length of pipe for an arbitrarily-shaped pipe or channel is given (White, 1991) as

$$\frac{-dP}{dx} = \frac{2Po\mu U}{d_h^2} \tag{2.8}$$

where U is the average velocity, for the case at hand x denotes the distance from the bulk fluid to the outer edge of the invading fluid (see Fig. 2.2), and d_h is the hydraulic diameter defined as $d_h = 4A/P_w$, where A is the cross-sectional area of the wetting fluid and P_w is the wetted perimeter (White, 1991). The Poiseuille number, $Po = C_f Re$, where C_f is the Fanning friction factor and Re is the Reynolds number associated with the diameter length scale (example: $Po = 16$

for a circular pipe). Solving for the loss of pressure due to viscous dissipation, ΔP_μ, for a given distance Δx gives

$$\Delta P_\mu = \frac{2Po\mu U\Delta x}{d_h^2}. \tag{2.9}$$

This general equation can be used for any geometry with the corresponding Po and d_h. Po is 14.38 for a rectangle with an aspect ratio of $\alpha = \delta/\lambda = 0.48$ (Shah and London, 1978) as is the case for the experiment used here.

Equation 2.9 can accommodate a number of increasingly complex geometries for channel cross-sections, from simple rectangular cross-sections (Fig. 2.4 d), to those that include the effect of contact angle on the shape of the upper meniscus (Fig. 2.4 e) and even tapered roughness posts (Fig. 2.4 f). For a model cross-section that includes the effect of the contact angle, $P_w = 2\delta + \lambda$ (the upper surface is a free surface; we assume no shear), and A is the rectangle's area minus the area of a circular segment (Fig. 2.4 e),

$$A = \lambda\delta - \frac{\lambda^2}{4}\Big(\frac{\frac{\pi}{2} - \theta}{\cos\theta} - \tan\theta\Big). \tag{2.10}$$

The hydraulic diameter is then

$$d_h = \frac{4\Big[\lambda\delta - \frac{\lambda^2}{4}\Big(\frac{\frac{\pi}{2}-\theta}{\cos\theta} - \tan\theta\Big)\Big]}{2\delta + \lambda}. \tag{2.11}$$

2.6 Invasion model

The driving capillary forces and resistive frictional forces are balanced to give an invasion equation $x = Dt^{1/2}$, where the constant of proportionality, D, is strongly dependent on the method for estimating the roughness channel geometry (e.g. Equation 2.9).

At any point in time, the frictional resistance (Equation 2.9) will be balanced against the driving force per unit area (Equation 2.7). Solving for the velocity, U, of the front edge of the invading fluid yields

$$U = \frac{\gamma d_h^2}{2Po\mu x}\Big(\frac{(2\delta + \lambda)\cos\theta - \lambda\sin\theta}{\delta\lambda}\Big). \tag{2.12}$$

Integration of Equation 2.12 leads to the motion of the fluid invasion,

$$x_h = \Big[\frac{\gamma d_h^2}{Po\mu}\Big(\frac{(2\delta + \lambda)\cos\theta - \lambda\sin\theta}{\delta\lambda}\Big)\Big]^{1/2} t^{1/2} + x_0. \tag{2.13}$$

where t is the time it takes for the edge of the fluid to travel the distance x along the textured surface (see Fig. 2.2), the subscript h denotes the use of hydraulic diameter to approximate the frictional resistance. The lower boundary for the roughness driven invasion is $x_0 = \kappa^{-1}$, where κ^{-1} is the capillary length given by $(\gamma/\rho g)^{1/2}$. Even on a smooth surface the wetting front will move up by a height of κ^{-1}.

It is assumed that the roughness elements have vertical sides with perfectly flat tops. This governs the shape of the interface. For roughness elements that are

not flat-topped (such as rounded spikes), the deviation of the surface from vertical will increase the cross sectional wetting area. This can easily be accounted for by adding a factor, θ', to the value of the static contact angle in Equations 2.10 and 2.11, where θ' is the angle by which the roughness element's wall deviates from vertical (see Fig. 2.4 f).

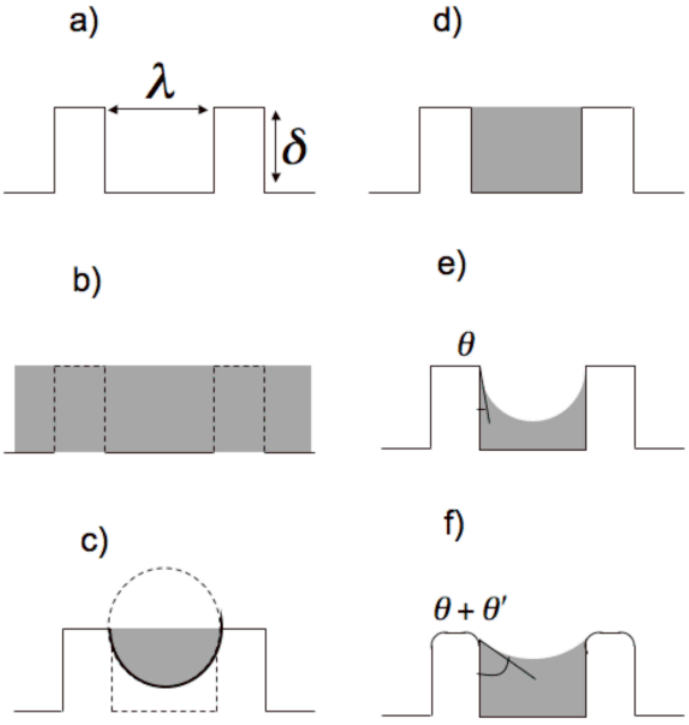

Figure 2.4: Various cross-sectional channel flow models used to estimate viscous dissipation. The solid line represents the shape of the ideal rough surface (height δ, width λ), the shaded region is the fluid. a) The rough surface, no fluid; b) Poiseuille film flow; c) Hagen-Poiseuille half-pipe flow; d) Hydraulic diameter approximation, rectangle; e) Hydraulic diameter, static contact angle off the vertical wall; f) Hydraulic diameter, static contact angle off tapered walls where θ' is the angle of the wall.

2.7 Other relevant fluid models for finding the frictional resistance

It is important to determine how much of the complexity of the roughness geometry should be incorporated into the model. The hydraulic diameter was thus compared to two other commonly used models for simplifying the flow geometry: Poiseuille (free surface) film flow that effectively ignores the effect of roughness on viscous dissipation, and Hagen-Poiseuille half-pipe flow that resembles the traditional Washburn (1921) model.

2.7.1 Poiseuille film flow approximation

The viscous force per unit area can be estimated from the classic Poiseuille law for a liquid film on a plane,

$$\Delta P_{\mu} = 3\mu U x/\delta^2, \tag{2.14}$$

where δ is assumed to be the film thickness.

Equation 2.14 ignores flow dissipation caused by the presence of the roughness cylinders and only accounts for no-slip condition along a smooth plate (see Fig. 2.4 b). Equating the driving capillary pressure (Equation 2.7) to the Poiseuille viscous resistance (Equation 2.14 instead of Equation 2.9) yields

$$x_P = \Big[\frac{2\delta^2\gamma}{3\mu}\Big(\frac{(2\delta+\lambda)\cos\theta - \lambda\sin\theta}{\delta\lambda}\Big)\Big]^{1/2} t^{1/2} + x_0, \tag{2.15}$$

where the subscript P denotes the use of the Poiseuille film flow approximation for frictional resistance.

2.7.2 Hagen-Poiseuille half-pipe flow approximation

Just as a capillary tube can be used to represent a simple pore in porous media, a simple cylindrical half-full-pipe flow can be used to model a single "roughness" channel. The no-slip boundary is applied along the entire semi-circular perimeter; no sheer is assumed for the flat surface.

The average velocity in a half-full cylindrical pipe is conveniently equal to the average velocity of a full cylindrical pipe, i. e. Hagen-Poiseuille flow. The viscous force per unit area is (White, 1991)

$$\Delta P_{\mu} = 8\mu U x/\delta^2, \tag{2.16}$$

where the radius of the pipe has been approximated by the height of the obstacles, δ (see Fig. 2.4 c). This approximation may be more adequate in naturally textured surfaces (e.g. rock) than for an engineered surface such as shown in Fig. 2.1, because natural systems are likely to have less severe vertical edges. A downfall of this method is that a pipe flow approximation will become less accurate for systems with obstruction heights not comparable to half-width between obstructions. The experiment presented here has $\delta = 1.2\mu m$ and half-width distance, $\lambda/2 = 1.25\mu m$.

Again, balancing the viscous force per unit area to the capillary pressure leads to a similar square root of time diffusion equation,

$$x_{H-P} = \Big[\frac{\gamma\delta^2}{4\mu}\Big(\frac{(2\delta+\lambda)\cos\theta - \lambda\sin\theta}{\delta\lambda}\Big)\Big]^{1/2} t^{1/2} + x_0. \tag{2.17}$$

where the subscript $H - P$ denotes the use of the Hagen-Poiseuille pipe flow approximation for the frictional resistance term. Note that the contribution to the diffusion coefficient by pipe flow, Equation 2.16, is always smaller than that by film flow, Equation 2.14; this is expected as vertical walls present increased viscous friction compared to a film.

2.8 Comparison to experiment

The proposed flow models, Equations 2.13, 2.15 and 2.17, was tested against experiments by Bico *et al* where a rough microstructured surface (Fig. 2.1) was brought into contact with a reservoir of silicon oil. The upward rate of fluid invasion into the rough surface is not dependent on surface orientation (Cazabat et al., 1986; Bico et al., 2001). Fig. 2.5 compares the experimental data of Bico *et al* (2001) with each of the three theoretical equations (Equations 2.13, 2.15, and 2.17).

Values for liquid properties taken from Bico *et al* (2001) were used to calculate the diffusion coefficients for Equations 2.13, 2.15, and 2.17. Surface tension, $\gamma = 20.6 \times 10^{-3} N/m$; density, $\rho = 950 kg/m^3$; advancing contact angle, $\theta = 0$; dynamic viscosity, $\mu = 16 \times 10^{-3} Pa - s$; height of the cylinders, $\delta = 1.2 \times 10^{-6} m$; radius of cylinders, $R = 0.5 \times 10^{-6} m$; and distance between cylinder edges, $\lambda = 2.5 \times 10^{-6} m$ (separation between cylinder centers $= \lambda + 2R$).

Values for each diffusion coefficient, D, correspond to the slope of the curves in Fig. 2.5 and are listed on the figure. The data corresponds to a curve with a functional dependence of $t^{1/2}$ with a slope of $0.027 \times 10^{-4} mm - s^{-1/2}$. The model

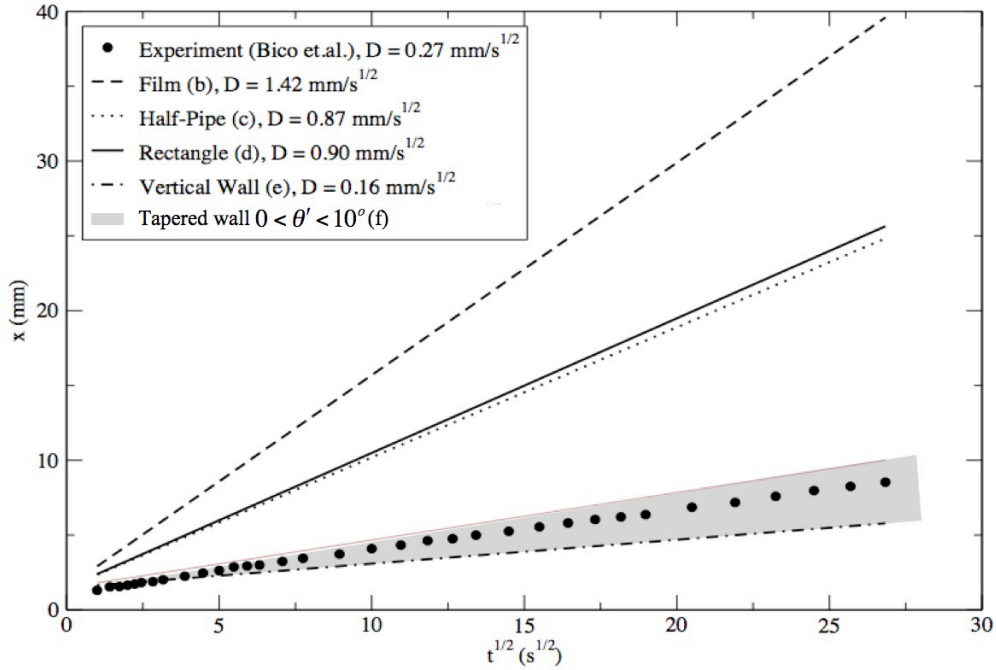

Figure 2.5: Data acquired by Bico *et al* (2001). Data and models of the form $x = Dt^{1/2} + x_0$ where D, the diffusion coefficient equals the slope of the line. Corresponding geometry illustrations from Fig. 2.4 are included in the legend. the gray shaded area shows the range of values for D for tapered wall angles of $0° < \theta' < 10°$.

that best fits the data is the model using a hydraulic diameter representation of the surface geometry corresponding to Fig. 2.4 f. The gray shaded region of Fig. 2.5 corresponds to values of θ' ranging from 0° to 10°. The data best fit corresponds to $\theta' = 7°$.

2.8.1 Discussion

Two notable discrepancies between the theory and the experimental data are the slope and the y-intercept in Fig. 2.5. The slope (i. e. diffusion coefficient) is the concern of this paper. Experimental artifacts possibly affecting the y-intercept were not discussed in the original manuscript (Bico, 2001). Data fit with a linear regression gives a positive y-intercept equal to $1.2mm$. The theory presented here gives a value $x_0 = 1.5mm$ for the y-intercept, corresponding to the theoretical capillary length.

Regardless of the geometry used for approximating fluid friction, Equations 2.13, 2.15 and 2.17 result in diffusion laws of the form $x \propto t^{1/2}$, having the same functional time dependence as the experimental findings of Cazabat and Cohen Stuart (1986) and the theoretical prediction of Bico *et al.* based on energy (Bico, 2001). The half-pipe flow model predicts slower movement than the simple Poiseuielle model because the pipe geometry provides for greater contact area, although it still doesn't account for the rectangular shape of the cylinder edges. If the rough texture is not completely filled in, or the half-separation between cylinders is significantly greater than the cylinder heights, the half-pipe model will over estimate the invasion rate. The effective hydraulic diameter approximation provides a more realistic boundary condition than film or pipe flow.

The hydraulic diameter approximation fits the data best. The shaded region in the figure shows model results for a range of tapering angles ($0^\circ < \theta' < 10^\circ$) for the roughness elements. No wall taper (vertical walls and flat tops, $\theta' = 0^\circ$)

under-predict the fluid cross-sectional area and thus the diffusion coefficient. Even a maximum taper of 10° gives a reasonable fit, with the best model fit for $\theta' = 7°$. However, a precise match given for a specific value of θ' does not not necessarily suggest that the roughness elements shown in Fig. 2.1 had a tapered edge of 7°. Some discrepancy between data and model should be expected from unaccounted-for physical mechanisms and the effect of various simplifying assumptions. There remain several unaccounted-for features in the theoretical analysis presented here.

The driving force was assumed to be a constant capillary force governed by the liquid-gas interface curvature described by the height and width dimensions of an idealized rough surface. The method for finding curvature, and therefore strength of capillarity, is unique to this analysis. However, this simplification does not allow for a changing shape of the advancing invasion fluid front.

Fluid dynamics on a very small scale is far from being completely understood. It is unknown if a capillary free-surface experiences shear forces that would significantly alter the velocity field. Here, no-slip solid boundaries and no-shear free-surface fluid boundaries have been assumed.

This problem has been treated completely as a two dimensional problem and any motion of the fluid normal to the surface has been ignored. However, it was determined that the time to fill (upwards) the space between the cylinders slows the overall horizontal flow a negligible amount since the interesting spreading distances are much larger than the height of the cylinders.

All of the viscous resistance models presented here were estimated using channelized flow instead of flow involving individual roughness elements. Immersed

objects, such as cylinders, provide a frictional drag which even at low Reynolds numbers creates a wake behind each object. This represents an additional loss of energy, which has not been taken into account.

While attention to these assumptions would improve accuracy, the model fit is very good and significantly better than that by more commonly used simpler flow geometries.

2.9 Implications of theory

The theoretical model presented here for the invasion process implies consequences as well as restrictions for spreading and non-spreading conditions that depend on the contact angle. Equations 2.13, 2.15, and 2.17 state that the spreading rate will depend only on contact angle, surface tension, viscosity, and the surface geometry (in this idealized structure: height, width, and separation of the cylinders). It may be interesting to note that the diffusion laws derived here do not depend on fluid density because this is a regime where the gravitational effect was considered negligible and the inertial terms are zero.

Perhaps the most striking consequence of the theory is that it predicts bounds on the condition for spreading that depend on the static contact angle as measured on a smooth surface. A critical contact angle, θ_c, exists at which neither spreading nor receding will occur. While for a smooth surface the critical angle is assumed to be 90°, for a rough surface θ_c depends on the roughness. Setting Equation 2.12

equal to zero, one arrives at the critical contact angle

$$\theta_c = \arctan\Big(\frac{2\delta}{\lambda} + 1\Big). \tag{2.18}$$

If θ is larger than θ_c, the fluid will not invade; if θ is smaller than θ_c, the fluid will invade. This has the surprising consequence that one need only know the contact angle and the height and separation of the roughness cylinders to determine if a fluid will spread on that surface. Equation 2.18 ignores external forces that can also drive spreading (example: a large drop will always spread due to gravity).

The argument in the arctan of Equation 2.18, $((2\delta/\lambda) + 1)$, is always between 1 and ∞, which means that the critical contact angle will always be between 45° and 90°. Fluids with a static contact angle $\theta < 45°$ will spread regardless of the surface structure. The theory presented here does not apply to a hydrophobic case ($\theta > 90°$), however it is already known that a hydrophobic interaction becomes more hydrophobic on a rough surface. If $45° < \theta < 90°$ the condition of spreading or receding will depend on the structure of the rough surface (i.e. the height, width and separation of the rough bumps). This means that theoretically, before knowing the structure of a rough surface, it is possible to predict the general behavior of the fluid on that rough surface by first observing if the static contact angle on a smooth surface of the same material lies outside of the 45 to 90° region.

2.10 Conclusion

The physical mechanism causing spreading on natural rough surfaces has yet to be completely understood and quantified. Here, a theoretical description is presented for a proposed physical mechanism responsible for liquid spreading on a rough surface. Using the model presented here, the rate of liquid spreading can be predicted given the fluid properties and geometry of the surface roughness. It is the nature of roughness in natural systems to be random and complex, making quantification of surface roughness difficult. However, this model has been shown to work very well for an idealized geometry. Even for a natural rough surface, idealizing the structure may provide a good approximation.

The model presented here was developed using the following understanding. A rough surface provides a means for forming curved liquid-air interfaces that produce capillarity. At very small scales, where gravity is not dominant, capillarity can be solely responsible for driving fluid movement. This is assumed to be the case for fluid invasion into roughness. Viscous friction within the fluid and along the boundaries of the solid opposes motion. The balance of these two forces is used to derive the equation of motion. A critical angle is identified which places bounds on the spreading behavior; fluids with a static angle (on a smooth surface) that is less than 45° will spread regardless of the surface roughness on the same material.

We thank Dr. José Bico for the use of his experimental data, Zachary Wiren for the many conceptual discussions that led to improving the invasion theory and the National Science Foundation (Grant 0449928) for financial support.

2.11 References

Bico, J., Tordeux, C., Quéré, D., 2001. Rough Wetting, Europhysics Letters, 55: 214-220.

Burlatsky, S.F., Oshanin, G., Cazabat, A.M., Moreau, M., 1996. Microscopic Model of Upward Creep of an Ultrathin Wetting Film, Physical Review Letters, 76: 86-89.

Cazabat, A.M., Cohen Stuart, M.A., 1986. Dynamics of Wetting: Effects of Surface Roughness, Journal of Physical Chemistry, 90: 5845-5849.

Quéré, D., 2002. Rough Ideas on Wetting. Physica A., 313: 32-46.

Shah, R.K., A. L. London, A.L., 1978. Advances in Heat Transfer, Academic Press, New York.

Washburn, E.W., 1921. The Dynamics of Capillary Flow, Physical Review 17: 273-283.

Wenzel, R.N., 1936. Resistance of Solid Surfaces to Wetting by Water. Industrial Engineering Chemistry, 28: 988-994.

White, F.M., 1991. Viscous Fluid Flows, McGraw-Hill, Boston.

Chapter 3 – An Experimental Investigation of Droplet Flow

K.M. Hay[1], D. Schwartz[1] , M.I. Dragila[2]

[1]Department of Physics, Oregon State University, Corvallis, Oregon

[2]Department of Crop and Soil Sciences, Oregon State University, Corvallis, Oregon

To be submitted:

Water Resources Research Journal

3.1 Abstract

While the hydrologic community is generally in agreement that fluid can travel through fractures in the vadose zone even when the matrix is unsaturated, there is still much to understand about the physics of fluid movement in the fractures. Field investigations show that two-phase movement in fractures can be quite erratic, changing paths over time and temporally varying in transmissivity. Laboratory investigations have identified at least three modes of flow, free surface films, droplets (liquid bridges) and rivulets. This highly variable behavior makes predictive modeling of flow in fractures in the vadose zone highly challenging. Since small scale fluid phenomena can greatly affect large scale transport behavior, understanding the physics controlling the small scale behavior is paramount to successful predictions of large scale transport processes. This manuscript investigates the movement of droplets between parallel walls. Presently, the kinematics of fluid droplet movement is thought to depend solely on gravity, capillary and viscous forces. While it is known that roughness changes the liquid-solid-gas contact angle, the role of roughness on droplet movement dynamics has not been investigated. Surface roughness may affect capillary and viscous forces. Presented here are results from experiments where the terminal speed of droplets was measured as a function of glass plate roughness. The advancing contact angle was adjusted for a dynamic effect and the nature of rough surfaces to maintain a wet layer, this resulted in improved modeling. Further considerations for improving predictions, which include allowing for internal droplet flow dynamics, are suggested.

3.2 Keywords

fluid transport, dynamic contact angle, roughness

3.3 Introduction and Background

Fluid movement in rock fractures can take on several forms including films, rivulets and droplets (Su et al., 2004); here the focus is on droplet flow, which is a liquid bridge between parallel plates. Ability to predict speed of droplets is relevant to environmental and industrial applications including fluid contaminant transport in unsaturated rock fractures.

Glass is commonly used to model rock in transport simulations. It has been observed that the speed of droplets moving down smooth glass fractures is significantly different than the speed down rough, porous fractures (Steele, 2004). Some theories for droplet speeds moving between parallel surfaces incorporate a dynamic advancing contact angle (Hoffman, 1975; Hoffman, 1983). Hoffman proposed that the contact angle of a three-phase interface will increase as a function of interface velocity. This concept was used to successfully explain the suppression of droplet speed in smooth glass parallel plates (Dragila and Weisbrod, 2003). Their approach involves the traditional Navier-Stokes equation reduced for a steady parallel plate flow and accounts for a pressure gradient due to the curved fluid-air interfaces at the front and back of the droplet (capillarity) across the droplet length. The same approach does not completely explain droplet speed on rough surfaces, which are faster. It is known that roughness changes the liquid-solid-gas contact angle (Wen-

zel, 1936). Roughness may also affect viscous forces by modifying the internal flow. The precise nature of the overall effect of roughness on the parallel plate system is not known.

In the following sections, a mathematical description of a moving droplet is derived. Then results from experiments of droplet speed on inclined rough parallel plates are presented which serve to refine the predictive relationships. The best speed predictions are approximated through a Navier-Stokes approach for a two dimensional infinite sheet of fluid between parallel plates and incorporate a pressure gradient over the length of the droplet imposed by capillarity at the advancing and receding edge. Additionally, the problem is made nonlinear with a dynamic advancing contact angle. An adjustment is proposed to the advancing contact angle due to the nature of rough surfaces to maintain a wetted layer. The deviation between theory and experiment is further discussed with a conceptual model for the internal dynamics of the droplet.

3.4 Theory

A droplet is a liquid bridge suspended between parallel plates. A two dimensional cross section of the droplet might look like Fig. 3.1. The advancing contact angle, θ_A and receding contact angle, θ_R are allowed to be different, $u(y)$ is the x-direction velocity, $2b$ is the aperture, L is the length of the droplet and the system is inclined with respect to the horizontal by the angle α.

An equation for the speed of a droplet is derived from the Navier-Stokes equa-

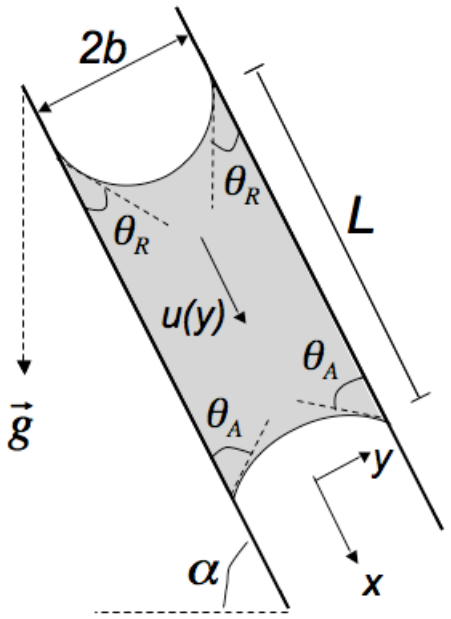

Figure 3.1: A two-dimensional cross section sketch of a droplet in the $x-y$ plane.

tions, applying the following simplifying assumptions. The droplet is treated as a wide and long plug. The droplet length is much greater than the fracture aperture ($L >> 2b$). This assumption ignores the dynamical effects caused by the larger curvature of the droplet in the plane parallel to the plates ($x-z$ plane), so the droplet flow can be reduced to two dimensions, as shown in Fig. 3.1. The expression for the velocity profile of a droplet is derived from the x-momentum Navier-Stokes equation assuming constant density and viscosity. Assuming steady state, fully developed flow with a velocity $u(y)$ in the x-direction, the reduced relevant equation is

$$\mu\left(\frac{\partial^2 u}{\partial y^2}\right) = \frac{\partial P}{\partial x} - \rho g_x, \tag{3.1}$$

where μ is the dynamic viscosity, $\partial P/\partial x$ represents a pressure gradient between the front and back of the flow, ρ is the fluid density, and g_x is the force due to the gravity in the x-x component of the gravitational force. If the right side of Equ. 3.1 is constant, there is a solution to this second order differential equation that requires two boundary conditions. These are assumed to be (1) a no-slip condition ($u = 0$) at $y = \pm b$ and (2) a maximum velocity ($\partial u/\partial y = 0$) in the middle of the aperture, at $y = 0$. The velocity is

$$u(y) = \frac{\frac{\partial P}{\partial x} - \rho g_x}{2\mu}(y^2 - b^2). \tag{3.2}$$

The average velocity is

$$\langle u(y) \rangle = \left(- \frac{\partial P}{\partial x} + \rho g_x \right) \frac{b^2}{3\mu}. \tag{3.3}$$

In the case of a droplet, the pressure gradient is generated by capillary hysteresis at the advancing and receding edges of the droplet, given by the Young-Laplace Equation,

$$\left(\frac{\partial P}{\partial x} \right)_c = \frac{\gamma}{L} \left(\frac{1}{R_A} - \frac{1}{R_R} \right), \tag{3.4}$$

where γ is the surface tension, L is the length of the droplet, and R is a radius of curvature for the advancing (A) and receding (R) edges of the droplet. With substitutions into Equ. 3.4 for the radii of curvature (through geometrical analysis

and assuming a circular meniscus cross-section),

$$R_i = \frac{b}{\cos\theta_i}, \tag{3.5}$$

where i is either A or R. We can further assume that the receding contact angle is zero because droplets leave a thin film behind them on the surface (Bico and Qu*éré*, 2004); the mass loss of fluid due to this thin film was ignored. The average droplet velocity is,

$$\langle u(y)\rangle = \frac{b^2}{3\mu}\left[\frac{\gamma}{Lb}(\cos\theta_A - 1) + \rho g \sin\alpha\right]. \tag{3.6}$$

According to De Gennes (1990), the advancing contact angle experiences a kinematic deformation that is strongly dependent on the droplet speed through the relationship,

$$Ca = \frac{u\mu}{\gamma} = \epsilon(\theta_A)^3, \tag{3.7}$$

where Ca is the dimensionless capillary number, u is the speed of the advancing interface and ϵ is an empirical constant of proportionality taken to be 0.005 (De Gennes et al., 1990; Dragila and Weisbrod, 2003). The average droplet speed, Equ. 3.6, becomes nonlinear when the contact angle allowed to be dynamic in this way. It was assumed that this dynamic effect was additional to the static contact angle already established between the droplet liquid and fracture solid, so that the

advancing contact angle for a droplet is actually,

$$\theta_A = \theta_S + \left(\frac{Ca}{\epsilon}\right)^{1/3}, \tag{3.8}$$

where θ_S is the static contact angle.

The derivation above is for laminar (creeping) flow. Deviations from the speed predicted by Equ. 3.6 would be expected for high Reynolds numbers. The Reynolds number is a ratio of inertial forces to viscous forces, and is used to identify the transition of a flow from laminar to turbulent. It is also used to classify similar flow behaviors. For simple flows, the Reynolds number reduces to

$$Re = \frac{\rho v l}{\mu}, \tag{3.9}$$

where ρ is the fluid density, v is the average velocity, l is a characteristic length and μ is the dynamic viscosity (Nunn 1989). Viscous forces dominate at low Reynolds numbers and inertial forces dominate at high Reynolds numbers. The selection of the characteristic length is somewhat subjective and intended to best represent the flow system. For a droplet, there are several lengths that may be considered characteristic and the ratio of inertial to viscous forces should be considered separately to identify a more appropriate Reynolds number. The ratio is,

$$Re = \frac{\rho v^2/l_i}{\mu v/(l_v)^2}, \tag{3.10}$$

where l_i is the characteristic length associated with inertial forces and l_v is the

characteristic length associated with viscous forces. For a droplet, l_i will be taken to be the length of the droplet, L, and l_v will be taken to be the half-width of the aperture, b. Then Equ. 3.10 reduces to the relevant Reynolds number for small lengths,

$$Re = \frac{\rho v b^2}{\mu L}. \tag{3.11}$$

3.5 Materials and Methods

Experiments were run to test the validity of the theoretical droplet speed, Equ. 3.6, with and without a dynamic contact angle effect. Physical parameters are varied, including surface roughness.

The experiment presented here was designed to measure the terminal velocity of a drop of water flowing between inclined glass plates of varying surface roughness. The plates were held parallel and at a constant, thin aperture. The surface of three sets of plates were roughened by sand blasting with three selected grades of sand. The fourth set is polished glass to represent a smooth surface. The surfaces of the glass were washed with non-residue soap and distilled water and scrubbed with a soft brush. Then they were rinsed with distilled water and allowed to air dry.

The aperture between the plates was created by eight metal shims of known thickness that were clamped in place. The thickness of the shims is taken to be the thickness of the aperture. In all cases, care was taken to place each clamp in the center of the shim, to avoid bending the glass and causing the aperture to vary.

Droplet speed was varied by changing the angle of inclination of the plates (i.e.

Inclination, α (degrees)	Range of observed droplet speeds (cm/s)			
	Smooth	Fine	Medium	Coarse
20	$2.0 - 2.8$	$2.4 - 2.9$	$6.7 - 12.0$	$4.4 - 8.2$
30	$3.2 - 4.3$	$3.9 - 4.9$	$10.2 - 16.5$	$6.0 - 10.2$
40	$3.9 - 5.6$	$5.6 - 6.8$	$13.8 - 16.4$	$6.9 - 9.6$
50	$4.8 - 7.7$	$7.7 - 15.0$	$14.5 - 21.8$	$8.2 - 11.8$
60	$6.2 - 9.6$	$17.8 - 27.5$	$19.6 - 27.0$	$10.6 - 14.2$

Table 3.1: Data table showing ranges of observed droplet speeds for high inclinations. Smooth represents polished glass plates. The designations Fine, Medium and Coarse refer to sandblasted glass with three selected grades of sand, not necessarily the degree of actual roughness.

the strength of the gravitational force). A range of apertures were tested at low inclinations, then a single aperture was selected ($0.081cm$) and tested over a range of inclinations (see Table 3.1).

For each set of plates and each aperture, a plate assembly was constructed. A drop of distilled water and $300ppm$ brilliant blue dye was deposited on the lower plate. For most of the trials the drop volume was initially $0.4mL$; the largest aperture required larger volumes to contact both of the plates. Shims were then placed around the edges and the top plate placed, then the assembly was completed by clamping plates together with shims in between.

Before the first trial, the path of the droplet was wetted by tilting the plates so that the droplet would flow slowly over the plates several times, forming a wetted path. For smooth glass the path did not stay wetted. A ruler attached to the top plate was used to measure the distance traveled by the droplet (usually $10 - 15cm$) and the length of the droplet (usually $1 - 3cm$).

For each trial, the droplet begins at the high end of an inclined supported plate assembly. The droplet was allowed to travel for at least ten centimeters before measurements were taken to ensure that terminal velocity had been reached. Droplets were injected one at a time. This process was repeated for each inclination of all four sets of plates. The parallel plates prepared were tested at 20, 30, 40, 50, and 60 degrees of inclination from vertical. Using a high definition video camera, mounted parallel to the plates, droplet length was measured, the droplet descent was timed and the distance traveled was recorded in order to calculate droplet terminal speed. Before each new inclination, the path of the droplets was wetted by injecting several drops of the test fluid, distilled water with $300ppm$ brilliant blue dye, into the high end of the plate assembly and allowing them to flow out the bottom.

3.6 Results

Droplet velocities are compared graphically to the velocities predicted by Equ. 3.6 (Fig. 3.2) and with inclusion of Equ. 3.8 (Fig. 3.3). To facilitate interpretation, a solid black line representing a one to one theory-experiment correlation is provided. For the purpose of constraining the number of free parameters, only aperture widths of $0.081cm$ are shown here. Four different surface roughnesses are included in the data: polished glass, and three sand blasted surfaces labeled fine, medium and coarse. Note that medium is not necessarily physically rougher than fine, it just represents the size of the abrasives used to create the sand-blasted texture, similar

for coarse to medium. The properties for a water-glass-air system are as follows: acceleration due to gravity, $g = 9.8m/s$; dynamic viscosity, $\mu = 0.001002kg/m-s$; surface tension, $\gamma = 0.0727N/m$; and density, $\rho = 1000kg/m^3$.

The static contact angle for all rough glass surfaces was assumed to be $\theta_A = 0°$, since the rough surfaces maintained a wetted layer of fluid throughout the experiments. This is a significant difference from the smooth glass surface which did not appear to maintain a wetted layer between experimental runs. The advancing contact angle for smooth glass surface was measured to be $\theta_A = 45°$. The length of the droplets, L, and the angles of inclination, α, were experimentally measured.

Equ. 3.6 predicts higher speeds than the data (Fig. 3.2), where as inclusion of the dynamic contact angle effect (Fig. 3.3) significantly improves the correlation between theory and observation. However, the discrepancy between theory and observation diverges for higher speeds (Fig. 3.4).

Fig. 3.4 plots the Reynolds number for each droplet calculated through Equ. 3.11 against the difference between the theoretical and experimental terminal speed (from Fig. 3.3), which incorporates the dynamic contact angle.

3.7 Discussion

Droplets travel faster on rough glass than on smooth glass. One reason for this is that rough glass, once wetted, maintains a wet surface which decreases the static contact angle to zero; smooth glass does not exhibit the same wetting behavior. Since curvature at the front and back of the droplet is responsible for the capillary

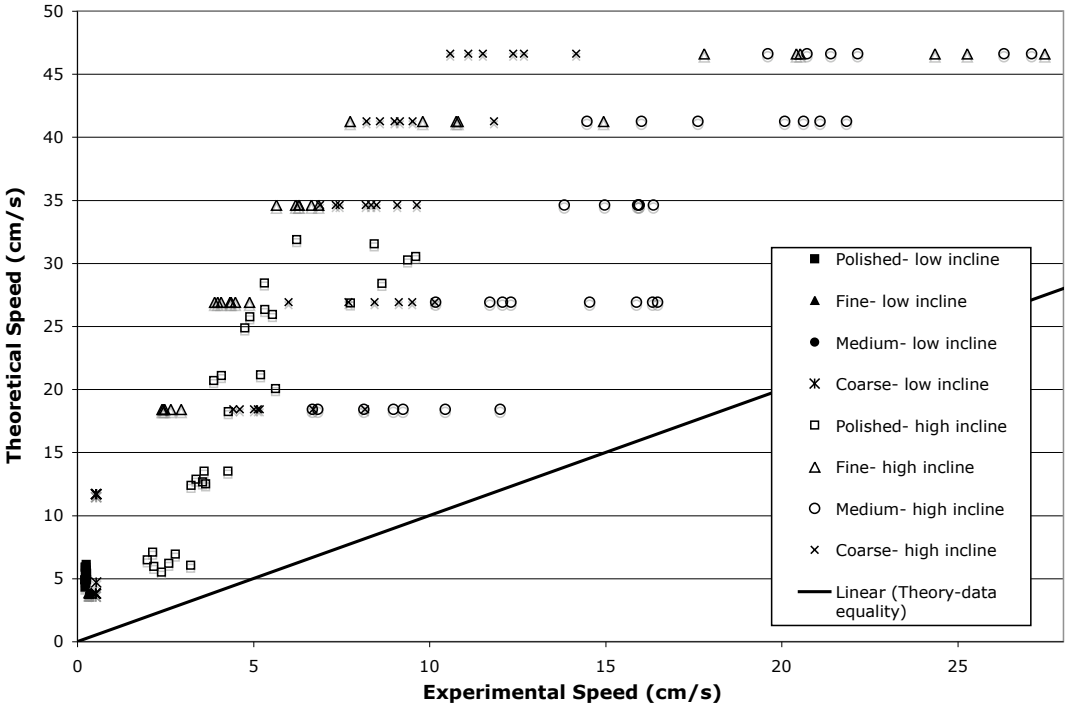

Figure 3.2: Speeds calculated with Equ. 3.6, not including the dynamic contact angle, are compared to data of inclined droplet experiments. Fine, medium and coarse refer to three different sand blasted glass surfaces.The solid black line represents a theory-experiment one to one correlation.

pressure gradient (according to Equ. 3.4). Because the receding angle is assumed to be zero, this pressure gradient will always resist the forward motion (unless the advancing and receding contact angles are equal, in which case it provides no change). So a decrease in the advancing contact angle predicts faster droplet speeds. However, increasing the droplet speed like this also increases the dynamic contact angle effect, which slows the droplet (through the same curvature argument). Here lies the nonlinearity of the system. Still, the roughness pre-wetted

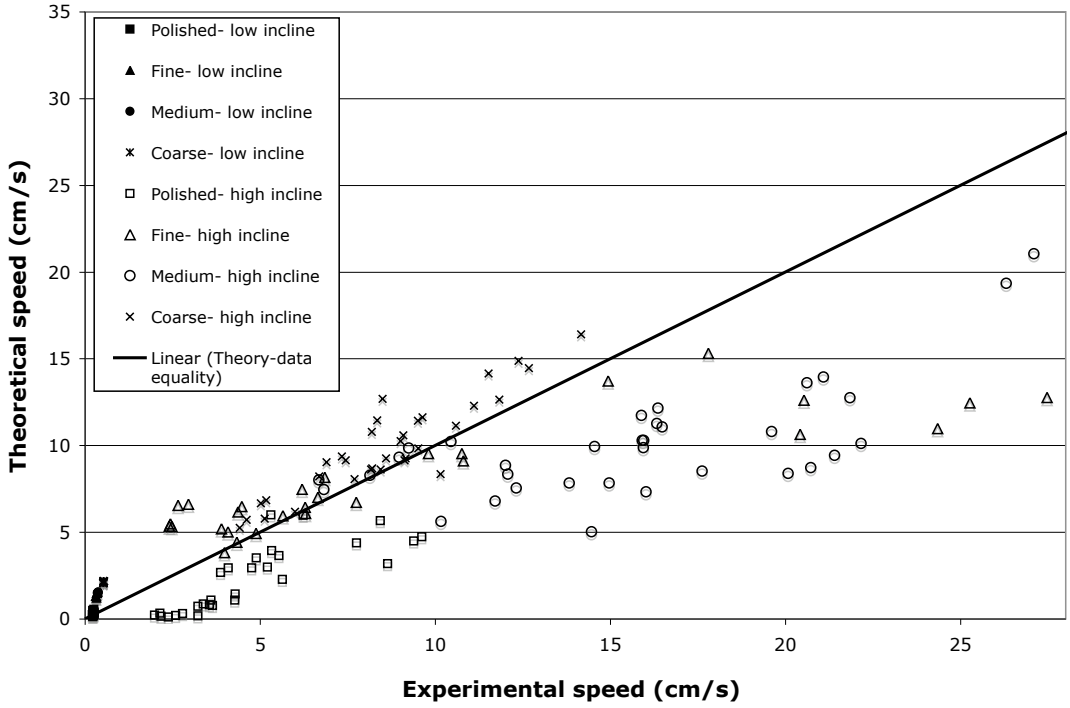

Figure 3.3: Speeds calculated with Equ. 3.6, including the dynamic contact angle, are compared to data of inclined droplet experiments. Fine, medium and coarse refer to three different sand blasted glass surfaces. The solid black line represents a theory-experiment one to one correlation.

adjustment to the advancing contact angle is a stronger effect for the range of observed speeds and appears to be responsible for increased speed of droplets on rough surfaces.

The deviation in the correlation between theory and experiment (Fig. 3.3) indicates that as the speed increases more energy is gained from the system than is accounted for in Equ.s 3.6 and 3.8. One possible explanation is elucidated by investigating the relationship between this deviation and the Reynolds number. The model tends to over-predict speed for low Reynolds number values and under-

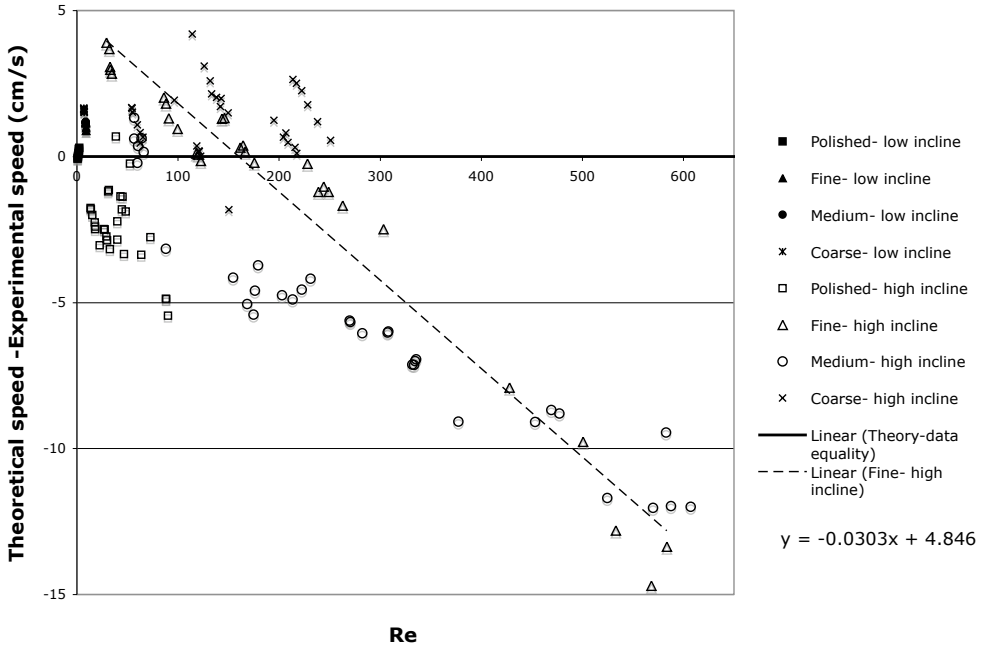

Figure 3.4: Reynolds numbers calculated with Equ. 3.11 are compared to the difference between theoretical speed and experimental speed. The theoretical speed was calculated with Equ. 3.6, incorporating the dynamic contact angle. Fine, medium and coarse refer to three different sand blasted glass surfaces. The solid black line represents a theory-experiment one to one correlation. A trend-line has been fit to one set of data (high inclined fine sand-blasted glass droplet speeds) and the equation for the trend-line appears beneath the legend.

predict speed for high Reynolds number values (Fig. 3.4). Accuracy of the model decreases with Reynolds number. Reynolds numbers are sometimes used to classify similar flow behaviors. This correlation points to the need for flow visualization to see if the internal dynamics of droplets are different at higher Reynolds numbers than at lower Reynolds numbers. Say for example, at lower Reynolds numbers the droplet exhibits a simple rolling motion over the whole area making two elongated swirls as in Fig. 3.5 and at higher Reynolds numbers, flow breaks up into

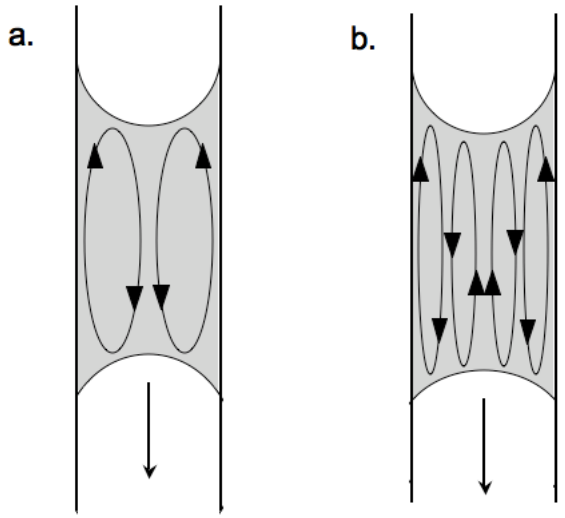

Figure 3.5: Illustration of possible internal flow dynamics of the droplet. Low Reynolds number droplets may have simpler dual rolling motion (a.) than higher Reynolds number droplets, allowing the middle of high speed droplets to move on a layer of rolling fluid (b.) and therefore move faster than predicted.

narrower separated swirls of flow, also shown in Fig. 3.5. Then the middle of the high Reynolds number droplet is allowed to slip along the lubricating outer fluid swirls. This would mean that the low Reynolds number droplet transfers frictional information across the aperture better than a fast moving droplet and the effect is higher Reynolds number droplets should move even faster.

Investigating this conceptual model further, a trend-line was fitted to the data set for droplets on fine sand-blasted glass at high inclinations, the linear equation is shown in Fig. 3.4. A correlation is implied,

$$v_{th} - v_{ex} = v_{slip} Re + v_{error} \tag{3.12}$$

where v_{th} is the theoretical droplet speed, v_{ex} is the experimentally observed droplet speed, v_{slip} is the negative slope of the trend-line and v_{error} is the vertical axis intercept. Solving for the experimental velocity,

$$v_{ex} = v_{th} + v_{slip}Re - v_{error}. \tag{3.13}$$

v_{error} is equal to $v_{th} - v_{ex}$ at $Re = 0$ and is a measure of the deviation between theory and experiment. This suggests that the experimental speed is equal to the current theory plus a factor that represents the added slip effect of having fluid flow over a fluid lubricating layer and minus a correction factor . The relationship is nonlinear, not just because of the dynamic contact angle but because of the new Reynolds number term which depends on the experimental speed. However, many forces in nature which affect motion depend on that motion (drag or air resistance for example). Applying this correction to the selected (fine- high incline) set of data provides significant improvement in theory-experiment match (Fig. 3.6).

3.8 Conclusion and Future Work

A droplet is just one of a the many types of flow seen in rock fracture fluid movement. A complete description of the complicated motion of a water droplet in a fracture geometry has not yet been fully identified. Presented here are the speeds of observed droplets compared to theoretical predictions. The theoretical prediction, a two-dimensional Navier-Stokes solution which accounts for gravity, capillarity,

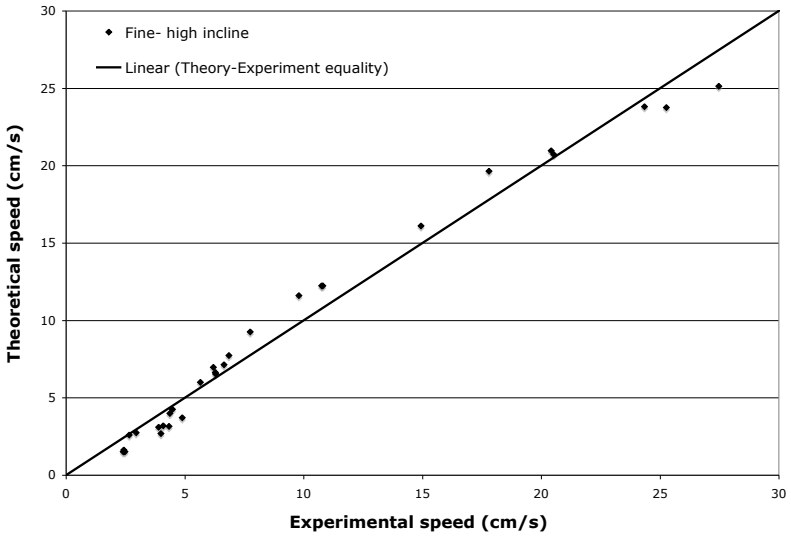

Figure 3.6: Observed droplet speeds on fine sand-blasted glass at high inclines are compared to corrected theoretical values governed by Equ. 3.13.

and viscosity is further improved by a dynamic advancing contact angle and an adjustment for pre-wetted roughness. However, even the best current speed predictions which include all of these mechanisms deviate from observed speeds and may be explained by unknown internal flow dynamics.

Internal droplet flow dynamics should be investigated with close-up flow visualizations. This may be done with florescent colloids, a black-light illumination and a high-speed camera to view droplets edge on. Experiments such as this may be used to classify the internal dynamics of droplets and eventually refine the

mathematical description of droplet flow and the corresponding speed predictions.

The study of the effect of texture on droplet speed is in its beginning phase. The eventual goal of this project is to better predict the speed of droplets moving in rock fracture systems. Understanding the physics behind this phenomenon will help build flow models for field applications. Other factors will have to be considered, such as absorption of fluid into the substrate, evaporation near the surface and chemical heterogeneity in the fluid and solid.

We thank the NSF (Grant 0449928) for financial support.

3.9 References

Steele, B., 2004. A Comparison of Theoretical and Experimental Capillary Droplet Speeds on Porous and Non-Porous Fracture Surfaces. Master of Environmental Soil Science Thesis, Oregon State University, Corvallis, Oregon.

Bico, J., Qu*é*r*é*, D., 2001. Falling Slugs. Journal of Colloid and Interface Science 243:262-264.

De Gennes, PG., Hua, X., Levington P., 1990. Dynamics of wetting: Local contact angles. Journal of Fluid Mechanics 212, 55-63.

Dragila, M.I., and Weisbrod, N., 2003. Parameters affecting maximum fluid transport in large aperture fractures. Advances in Water Resources 26: 1219-1228.

Hoffman, R.L., 1975. A study of the advancing interface I. Interface shape in liquid-gas systems. Journal of Colloid and Interface Science, 50(2): 228-41.

Hoffman, R.L., 1983. A study of the advancing interface II. Theoretical prediction of the dynamic contact angle in liquid-gas systems. Journal of Colloid and Interface Science 94(2): 470-486

Nunn, R.H., 1989. Fluid Mechanics. Hemisphere Publishing Corporation, New York.

Su, G.W., Geller, J. T., Hunt, J.R., Pruess, K., 2004. Small-scale features of gravity-driven flow in unsaturated fractures. Vadose Zone Journal 3:592-601.

Wenzel, R.N., 1936. Resistance of Solid Surfaces to Wetting by Water. Industrial Engineering Chemistry, 28: 988-994.

Chapter 4 – Intersection Rules for Droplets Encountering Fracture Intersections

K.M. Hay[1], M.I. Dragila[2]

[1]Department of Physics, Oregon State University, Corvallis, Oregon

[2]Department of Crop and Soil Sciences, Oregon State University, Corvallis, Oregon

To be submitted:

Water Resource Research Journal

4.1 Abstract

While it is generally accepted that fluid travels through rock fractures in the vadose zone, even when the matrix is unsaturated, there is still much to understand about the physics of fluid movement in the fractures. Field and laboratory investigations show that two-phase movement in fractures can be quite erratic, changing paths over time and transitioning between modes of flow. This highly variable behavior makes predictive modeling of flow in fractures highly challenging. Since small scale fluid phenomena can greatly affect large scale transport behavior, understanding the physics controlling the small scale behavior is paramount to successful predictions of large scale transport processes. This manuscript investigates the movement of fluid droplets through fracture intersections. An analytical function is derived to determine the distribution of liquid across a fracture intersection. The case of an initial droplet entering the system vertically downward and encountering an intersection of two forks is analyzed for antisymmetric situations. Input flow parameters, geometry of the system, capillary and gravitational forces are analyzed to predict volume and velocities of the output flows. Equations are further used as an upscaled analysis to investigate the spreading characteristics of a liquid plume in a fractured system. This initial study will permit future larger scale vadose zone models to account for pore-scale fluid phenomena that occur at intersections.

4.2 Keywords

rock fracture, intersection, droplet

4.3 Introduction

It would benefit many scientific communities to be able to predict fluid transport through unsaturated fractured rock regions in the vadose zone. Behavior of fluid through a fractured network is difficult to observe. Field investigations show that two-phase movement in fractures can be quite erratic, changing paths over time and temporally varying in transmissivity. Laboratory investigations have identified at least three modes of flow, free surface films, droplets (liquid bridges) and rivulets (Su et al., 2004). This highly variable behavior makes predictive modeling of flow in fractures in the vadose zone highly challenging. Since small scale fluid phenomena can greatly affect large scale transport behavior, understanding the physics controlling the small scale behavior is paramount to successful predictions of large scale transport processes. In order to model multiphase flow in complex systems of fractures, it is important to understand the basic physics that describes small scale fluid movement, especially in transitionary regions, such as intersections between fractures.

Wood et al. (2002) found that fracture intersections can serve as integrators of flow, flow pulses from above can interact at the intersection and change the frequency of the pulse. At the scale of a single fracture intersection, Dragila and Weisbrod (2004) performed experiments to study the evolution of a fluid droplet as it moved down a fracture and across a symmetric three-way intersection. The intersection can serve as a capillary barrier as the fracture aperture widens, holding fluid behind it until a critical mass (gravitational component) can overcome the

capillary barrier. Other observations included the transition of a droplet to two films or to a droplet and a film at the intersection.

Some numerical modeling approaches such as the method of volume of fluid (VOF) (Huang et al. 2005) and smoothed particle hydrodynamics (SPH) (Tartakovsky 2005) have successfully modeled intersection dynamics and reproduced experimental results. However, further simplified analytical formulas are needed. Computational modeling is useful in visualizing pore-scale fluid movement, but these models are not necessarily simple or inexpensive to upscale to large networks of fractures. To upscale, you still need to know the effects of fluid interaction with the fracture boundaries and intersections. For these reasons, some simple analytical rules (equations) would be powerful in predicting and testing various scenarios of intersections and systems of intersections.

In the sections to follow, an analytical function is derived to determine the distribution of liquid across a fracture intersection. The case of an initial droplet entering the system vertically downward and encountering an intersection of two forks is analyzed in general. Equations are further used as an upscaled analysis to investigate the spreading characteristics of a liquid plume in a fractured system. Some special cases of the predictive relationships are discussed for the purpose of categorizing behaviors.

4.4 Theory

Intersection rules (theoretical predictions of intersection fluid behavior based on input parameters) are derived for the case of a droplet moving vertically downward between parallel plates and as it moves across an intersection fork. A real fractured rock intersection network is extremely complex. The rock is porous and rough, the matrix can absorb fluids, evaporation can take place in the fractures, there may already be fluid trapped in the fracture system, fracture geometry varies and the interacting fluid, soil or rock may be chemically and physically heterogeneous. However, general behavior of fluid in fractures can be elucidated through simple models describing fluid interface evolution. This study may provide a framework for understanding the mechanisms controlling fluid distribution in fracture networks.

Geometric parameters known a priori are the angles at which the two branches exit the input branch and the aperture of all three branches. The geometry of a three way intersection is defined in Fig. 4.1. The intersection branch exit angles (β_i, where $i = 1, 2$ represents the two exit branches), are between 90 and 180 degrees. The half aperture width for all three branches is given as b_i ($0, 1$ and 2 represent the input, and two output branches respectively).

Assume that the volume of an incoming droplet, V_0, is known. We could instead use vertical length, L_0, because we are simplifying to a two dimensional problem. The receding contact angle is assumed to be zero because a film is left behind the droplet; the advancing contact angle, θ_A, is a variable in the problem and is

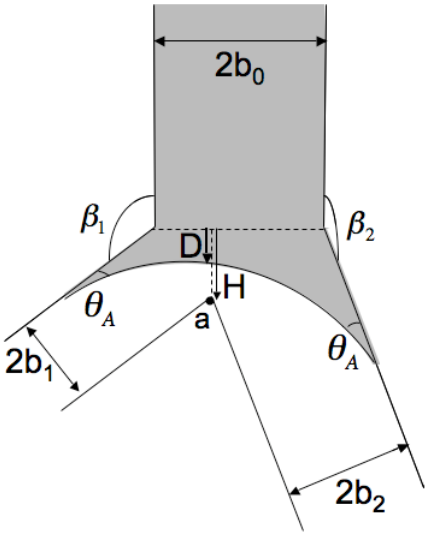

Figure 4.1: Geometric parameter definitions for a three-way intersection. Illustration not necessarily to scale.

allowed to be adjusted by a dynamic effect (Hoffman, 1975; Hoffman, 1983; De Gennes 1990).

A curved fluid interface creates a capillary force towards the inside of the curvature; the smaller the curvature, the stronger the force. As a droplet advances into an intersection, the aperture widens allowing the advancing radius of curvature to become greater, while the receding end experiences the same upward capillary force. In some cases, this change can be great enough so as to keep the droplet from penetrating into the intersection, the weight of the droplet cannot overcome the net capillary force upward. This phenomenon is called a capillary barrier. As discussed by Dragila and Weisbrod (2004), the intersection opening creates the possibility for a capillary barrier and for passage through the intersection, the

length of the droplet must satisfy

$$L_0 > \frac{\gamma}{\rho g}\Big(\frac{1}{b_0} - \frac{1}{R_{Ai}}\Big), \tag{4.1}$$

to overcome the capillary barrier, where R_{Ai} is the radius of curvature of the advancing interface during invasion of the intersection. This condition is derived through a Navier-Stokes analysis for a droplet (the speed of a droplet will be derived in the next section).

For an incoming droplet, there are two possible output modes, films or droplets, or a combination generated across an intersection. The relationship between the apex height, H, and the maximum invasion distance, D_{max} (which is related to the length required to overcome the capillary barrier) determine the output flow mode (see Fig. 4.1). If $D_{max} < H$, the output flow mode is two films; if $D_{max} > H$, the output flow mode is two (dual) droplets. Output films and criteria for overcoming the capillary barrier are discussed in Dragila and Weisbrod (2004). This paper focuses on dual droplet mode. It will be assumed in the following sections that the incoming droplet always touches the apex and two outgoing droplets are created from the incoming droplet. Sections 4.4.1 and 4.4.2 explain the *intersection rules*, then sections 4.5 and 4.6 demonstrate the ways in which these intersection rules can be applied in both small-scale and large-scale systems.

4.4.1 Intersection Rule One: Output Volume Ratio

When the advancing meniscus of the input droplet touches the apex (point "a" in Fig. 4.1), two new advancing interfaces form, one in each branch. The velocity of the two resulting fluid-air interfaces can be approximated through a Navier-Stokes equation analysis.

Fundamentally, flow of a droplet in a single fracture is governed by the Navier-Stokes equations:

$$\rho(\vec{u}\cdot\nabla)\vec{u} = \rho\vec{g} - \nabla P + \mu\nabla^2\vec{u}, \tag{4.2}$$

where ρ is the fluid density, $\vec{u}$ is the velocity vector, $\vec{g}$ is the acceleration due to gravity, P is the pressure, and μ is the dynamic viscosity. These equations can be reduced for the case of a droplet system ignoring internal flow dynamics and the oval shape of the droplet in the fracture plane. The pressure gradient is generated by the difference in curvature of the advancing and receding menisci, and calculated through the Young-Laplace equation. For steady state, Equ. 4.2 reduces to

$$0 = -\rho g \sin\alpha - \frac{\gamma}{L}\Big(\frac{1}{R_A} - \frac{1}{R_R}\Big) + \mu\nabla^2 u, \tag{4.3}$$

where γ is the surface tension, R_A and R_R are the radii of curvature for the advancing and receding menisci in the plane of he aperture, α is the fracture inclination from the horizontal, and L is the droplet length (Dragila an Wiesbrod, 2004). The advancing and receding curvatures are found geometrically, where the advancing contact angle is θ_A and the receding contact angle is assumed to be zero.

Droplet speed is then

$$u_{droplet} = \frac{b^2}{3\mu}\Big[\rho g \sin\alpha + \frac{\gamma}{L}\Big(\frac{\cos\theta_A}{b} - \frac{1}{b}\Big)\Big], \tag{4.4}$$

where b is the half-aperture.

Equ. 4.4 can be used to approximate the speed of the fluid-air interface as the droplet encounters the intersection. The speed of each interface is

$$u_i = \frac{b_i^2}{3\mu}\Big[\rho g \cos(\pi - \beta_i) + \frac{\gamma}{L_0}\Big(\frac{\cos\theta_A}{b_i} - \frac{1}{b_0}\Big)\Big], \tag{4.5}$$

where $i = 1, 2$ representing the two output branches and, as a first approximation, the length of the initial droplet, L_0, is used as the length over which the capillary pressure gradient is imposed (see Fig. 4.2). This equation is the result of a Navier Stokes analysis on droplet flow (liquid bridge between two plates), with a pressure gradient imposed over the length of the droplet caused by the curved interface (capillarity) at the advancing and receding edge. This technique has been used to mathematically describe droplet flow between glass plates (Dragila and Weisbrod, 2003). The fracture apertures $(2b_0, 2b_i)$ have been adapted to reflect a the change in geometry as the droplet passes form the incoming branch into one of the outgoing branches. $b_i^2/3\mu$ comes from the viscosity term (friction), this will allow for the speed of the fluid-air interface to increase due to an enlargement of the aperture or to decrease due to a narrowing of the fracture aperture. The term $\rho g \cos(\pi - \beta_i)$ represents the force due to gravity on a droplet flowing down the outgoing branch, this will allow for the speed of the interface to be affected by the inclination angle

of the outgoing branch. The last term represents movement of the fluid due to the pressure gradient imposed by capillarity on the front and back of the droplet fluid-air interface as it passes from one aperture to another.

Solutions to Equ. 4.5 for an intersection with two branches fall into three categories. When both interface velocities are positive ($u_i > 0$), competition of forces will govern how much fluid goes into each branch. A single negative interface velocity ($u_1 > 0,\ u_2 < 0$ or $u_1 < 0,\ u_2 > 0$)means that the entire incoming droplet will eventually flow only into the positive branch. When both branches give negative interface velocities ($u_i < 0$), the droplet will not proceed though the intersection.

Assuming conservation of mass, the ratio of liquid volumes entering each branch, $V_1 : V_2$ is determined by the flow rate (velocity times cross sectional area) ratio, which for a two dimensional system means that the volume ratio is

$$\kappa = \frac{V_1}{V_2} = \frac{u_1}{u_2}\frac{b_1}{b_2}, \tag{4.6}$$

where u_1 and u_2 is defined by Equ. 4.5. The volume of the original droplet is distributed according to the competition between gravity and capillary forces acting on the fluid interface at the entrance of each output branch. Thus, given the input droplet volume, V_0, the output volumes can be calculated,

$$V_1 = \frac{V_0}{(1+\frac{1}{\kappa})}, V_2 = \frac{V_0}{(1+\kappa)}. \tag{4.7}$$

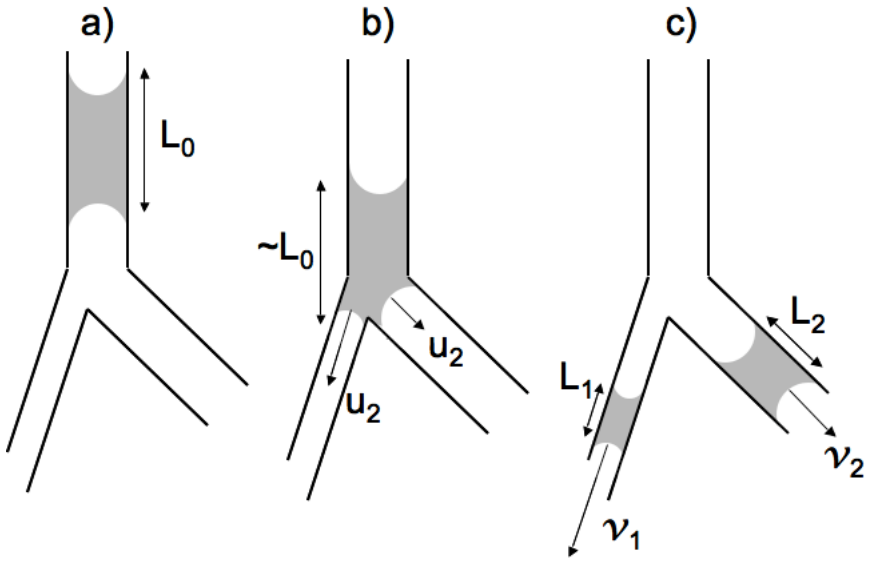

Figure 4.2: Sketch of a droplet of length L_0 progressing through an intersection, a) initial droplet, b) droplet length still approximated as L_0, interface velocities, u_i $(i = 1, 2)$, c) output droplets with terminal velocities, v_1 and v_2, and lengths L_1 and L_2. Illustration not to scale.

4.4.2 Intersection Rule Two: Output droplet terminal velocities

Using the volume ratio, one can calculate the length of the output droplets. Using the length one can calculate the terminal velocity which is the average velocity for a droplet between inclined parallel plates (Dragila and Weisbrod 2003). Specifically, the terminal velocity for each branch is given by Equ. 4.7 where L_0 becomes L_i and b_0 becomes b_i,

$$v_i = \frac{b_i^2}{3\mu}\Big[\rho g \cos(\pi - \beta_i) + \frac{\gamma}{L_i}\Big(\frac{\cos\theta_A}{b_i} - \frac{1}{b_i}\Big)\Big]. \tag{4.8}$$

Since in a two dimensional system, volume $V_i = L_i b_i$, then from Equ. 4.7, L_i can be expressed as

$$L_1 = \frac{L_0 b_0}{b_1(1+\frac{1}{\kappa})}, L_2 = \frac{L_0 b_0}{b_2(1+\kappa)}. \tag{4.9}$$

4.4.3 Intersection Rule Three: Condition for Output Volume Equality

A special case arises when the apertures and branch angles are in a three-way intersection are not necessarily the same, yet the output volumes are equal, $(V_1/V_2) = 1$ because the condition for output volume equality is $V_1 = V_2$. Going a little further with this point, most of the fluid will go toward the outgoing branch of aperture $2b_1$ as opposed to $2b_2$, if $(V_1/V_2) > 1$. Applying $(V_1/V_2) > 1$ to Equ. 4.6 gives the condition for majority of flow into branch 1,

$$\frac{b_2^2 - b_1^2}{b_2^3 - b_1^3} < \frac{1}{\cos\theta_A}\Big(\frac{1}{b_0} - \frac{L_0}{\gamma}\rho g \cos(\pi - \beta)\Big), \tag{4.10}$$

where b_0 and L_0 describe the incoming droplet and the angle $\beta = \beta_1 = \beta_2$. If this inequality was an equal equation instead the outgoing droplets would have equal volumes. The reverse inequality gives the condition for the majority of the fluid going toward the fracture of aperture $2b_2$. This condition is important in a system of multiple intersections, where it is desirable to know which direction is preferred by the plume of spilled fluid into a fractured rock system. Equ. 4.10 implies a condition under which a geometrically antisymmetric system ($b_1 \neq b_2$, $\beta_1 \neq \beta_2$)

can distribute volumes from the original droplet equally, as in a symmetric system ($b_1 = b_2$, $\beta_1 = \beta_2$). The inequality in Equ. 4.10, provides a way to determine which branch will yield the majority of the incoming liquid.

4.5 Droplet Separation Behavior

The next task is to use the formulas presented in sections 4.4.1, 4.4.2, and 4.4.3 to investigate the effect on flow distribution for a range of fracture intersection geometries. A simple case is discussed graphically to illustrate the effect of the initial conditions and geometric parameters on the output droplets. Values used for the fluid parameters approximately simulate an air-water-rock humid fracture system: viscosity, $\mu = 1.002 \times 10^{-3} Ns/m^2$, density, $\rho = 1000 kg/m^3$, fluid-air surface tension, $\gamma = 0.072 N/m$, and acceleration due to gravity, $g = 9.8 m/s^2$ and a dynamic advancing contact angle, $\theta_A = 15^\circ$.

Consider a simple symmetric case where all branches have the same aperture, say $b_0 = b_1 = b_2 = 1mm$. One of the branch angles is fixed at $\beta_1 = 3\pi/4$. The output volume is calculated as the second branch angle, β_2, is allowed to vary. Fig. 4.3 is a plot of V_1 and V_2 vs. β_2 in the valid region $\pi/2 < \beta_2 < \pi$. Due to the two-dimensionality of this system, L can be used as a surrogate for volume. Notice the total volume always adds up to the initial volume V_0 (here V_0 was normalized to 1 unit for simplicity). The angle and thus the strength of the gravitational force pulling the fluid into each branch controls output volume. V_1 (black line) decreases as β_2 increases and V_2 (grey line) increases. This is expected since with all the

apertures of the branches equal, the capillary forces are balanced and therefore don't affect the motion of either droplet, only the gravitational forces are the only driving forces remaining to affect the droplet's distribution. As the second branch angle increases, the gravitational component and the output volume increases in the second branch. At $\beta_2 = 3\pi/4 = \beta_1$ the two output volumes are equal due to symmetry.

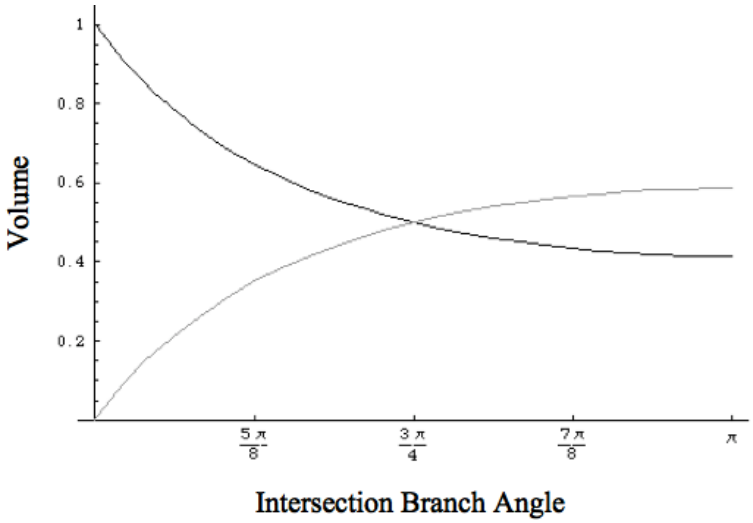

Figure 4.3: Output volumes, V_1 and V_2, are plotted against a variable intersection exit branch angle, in this case β_2. The units of volume are normalized such that the total volume for the two output droplets add up to 1 ($V_0 = 1$). The black line represents V_1 and the grey line represents V_2.

4.6 Upscaling to a System of Fractures

The usefulness of the intersection rules derived in the previous sections are used here to map the movement of fluid through a simulated fractured rock system of

intersections. The analysis was done using a computer modeling approach. For the numerical simulations presented, the three-way intersection system is used to approximate a four-way intersection where one of the possible outgoing branches would require fluid to flow against gravity (upwards); it is assumed that no fluid enters this upwards pointing branch. This is appropriate because any fluid that moves into an upward tilted branch, due to capillary forces, will eventually flow out of that branch and progress into one or divide into both of the other two downward titled branches. The input branch is no longer required to be lined up with gravity. β_i is measured form the vertical instead of the incoming branch. The kinds of intersection systems meant to be modeled by the computer programs are illustrated in Fig. 4.4; some geometric parameters and initial conditions can be adjusted.

Results demonstrate the usefulness of the intersection rules to analyze fluid distribution in a fractured subsurface. When fluid enters the system at some surface point, it will distribute throughout the system in response to competing forces which it encounters whenever an intersection is passed. The absorption of fluid into the rock walls is ignored in this study. Eventually, fluid droplets will stop moving downwards into the system because droplet length is insufficient to overcome capillary forces. For the simulation purposes order will be used to describe the number of intersections passed in the vertical direction. The lowest intersection order reached by the fluid may be translated into depth if the geometry of a system is known. The next three sections present graphical simulation results. Fig. 4.5 is an illustration of a symmetric intersection system that allows fluid

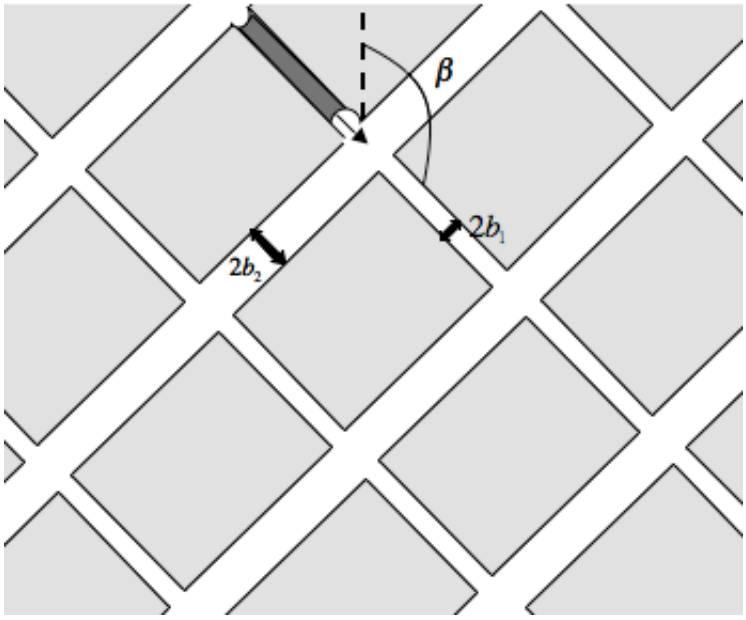

Figure 4.4: This is the kind of intersection system modeled by computer simulations. The aperture of all parallel fractures are equal, so there can be up to two different fracture apertures in the system, $2b_1$ and $2b_2$. All fractures are tilted with respect to vertical by an angle β, this branch exit angle is always between 90° and 180°.

droplets to flow down, separating equally at each intersection until the droplets become small enough that they can no longer overcome gravity. Again, the fluid values approximately simulate an air-water-rock humid fracture system a value is chosen for the advancing contact angle, $\theta_A = 15°$. It should be noted that in reality, the advancing contact angle will change with speed, a nonzero value was assumed simply to make the capillary force on the droplets nonzero, as it would be with a dynamic contact angle. Incorporating the dynamic contact angle into this study would make the speed of the fluid-air interfaces and the terminal speed of

the droplets nonlinear, this is a level of complexity that will be necessary when it comes to predicting specific real situations but for now, hinders the main purpose of this manuscript, which is to discover the general affect pore-scale fluid physics has on large scale fracture systems.

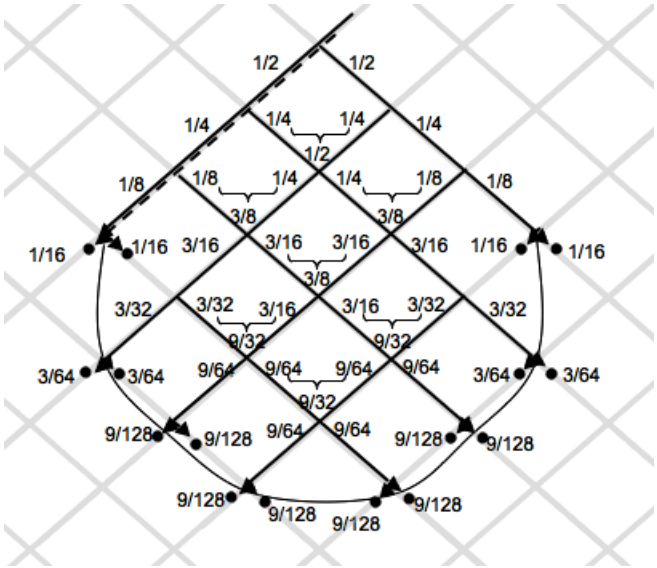

Figure 4.5: An illustration of how fluid is distributed within a symmetric two-dimensional intersection system when the fluid divides in half each time it encounters an intersection. The initial fluid entry point is at the top most intersection. This system was set up so that when fluid droplets become smaller than about 1/16 of the original droplet, they will penetrate no further and the stopping points are marked with black dots. Fractions denote how much fluid of the total comes out of each intersection branch. Brackets total the incoming droplets at intersections where there are two incoming droplets. The dotted line marks the edge of the plume front. A curved line draws where the droplets stop (the edge of the final plume). This diagram is later numerically simulated.

The last intersections crossed by the fluid droplets are drawn as black dots in Fig. 4.5. The imaginary curve made by connecting these dots is called the

maximum plume front. The first simulation (section 4.6.1) models the speed of the droplets taking the path denoted by a dotted line in Fig. 4.5. Section 4.6.2 presents a simulation that models the maximum plume front for symmetric systems like the one illustrated and the final program in section 4.6.3 models a maximum plume front for antisymmetric systems.

4.6.1 Plume Edge Extinction Order

Consider fluid traveling through a symmetric intersection system on the edge-most fracture, represented as a dotted line in Fig. 4.5. At every intersection encountered, the droplet will split and the resulting droplet that continues to the next intersection on the edge will contain half as much fluid. This process continues until the droplet is small enough to meet the stopping criteria, found by setting the terminal velocity (Equ. 4.8) equal to zero. This minimum length criteria, which will be different for different apertures and branch angles, is

$$L_i < \frac{\gamma}{\rho g \cos(\pi - \beta_i)}\Big(\frac{1}{b_i} - \frac{\cos\theta_A}{b_i}\Big), \tag{4.11}$$

where i specifies the branch where the droplet is located. When the final droplet stops moving downward, the last intersection passed is recorded and this is called the extinction order. While the droplets become smaller along this path their velocities decrease. Fig. 4.6 shows a plot of velocities of the droplets after passing each order (intersections downward). This is not a functional relationship, the

speed of the fluid is governed by its shape, amount and the geometry of the fracture, but these parameters are changed as the droplet decreases in size after each intersection crossing. For intersection systems with steeper branch angles (β), the droplets travel faster due to an increase in gravitational force and can progress through more intersections, and have a higher extinction order. Fig. 4.7 plots extinction order against branch angle for various apertures. This graph shows how the droplets can penetrate further into the system with steeper branch angles, at least on the edge of the plume. Two different apertures are shown on the graph. Larger apertures can also increase the extinction order because the upward capillary forces on the droplet are decreased with wider fractures.

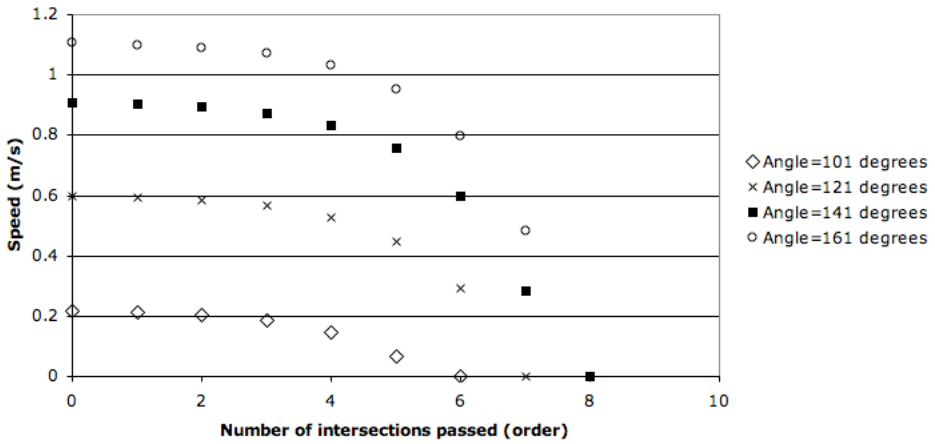

Figure 4.6: This graph records the speeds of droplets traveling on the edge of a plume (following the dotted line in Fig. 4.5). The fluid amount decreases by half each time it passes an intersection. The order for which the speed of a droplet is zero is called the extinction order. Angle refers to the branch angle β.

The program used to generate the plots in this section is included in appendix

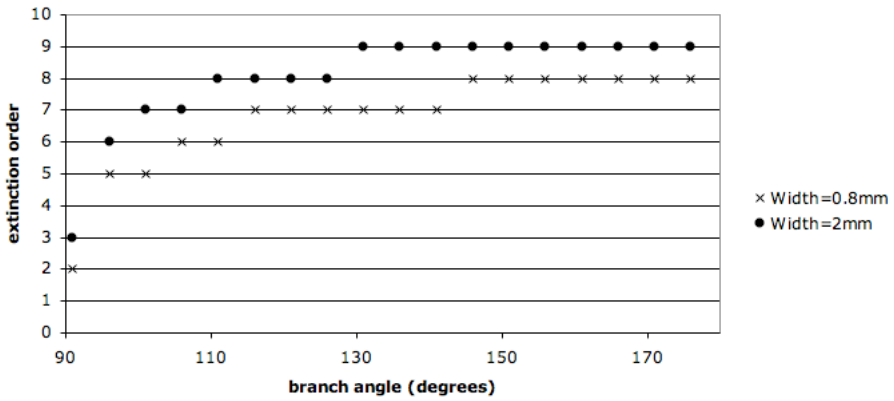

Figure 4.7: Extinction order plotted against branch angle, β, for two different apertures and for droplets taking the dotted line path (plume edge) in Fig. 4.5.

A.

4.6.2 Symmetric Maximum Plume Front Simulation

This section presents the graphical results of a computer program that replicates the illustration in Fig. 4.5. This program reproduces the edge extinction order from section 4.6.1, however, it does not include the information on terminal speed of the droplets after each intersection as that program does.

The program starts with an initial amount of fluid which enters at the surface of the intersection system and splits up equally every time it encounters an intersection. Droplets travel through the system until the minimum length criteria is met (Equ. 4.11. The location (number of intersections down and across) of the

last passed intersections are recorded and the results map out the maximum plume front .

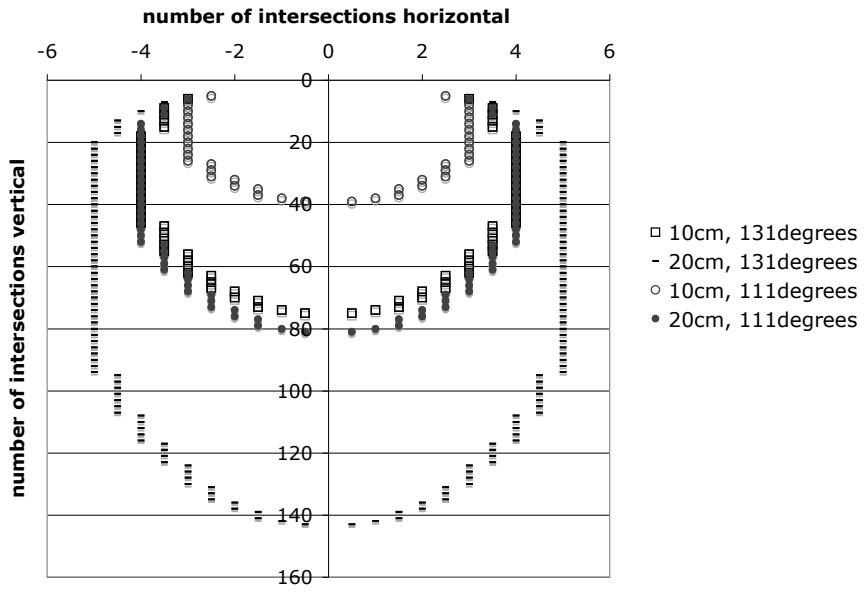

Figure 4.8: Graphed are computer simulated extinction orders in symmetric intersection systems for two input droplet lengths and two branch angles. This graph does not translate to a spatial comparison of systems with different branch angles because steeper angles give a different spatial map (more spread out vertically and less spread out horizontally). This is only a comparison of the number of intersections passed in each case. This simulation is an analogy to the diagram in Fig. 4.5.

Fig. 4.8 shows the result of flow distribution in a the symmetric intersection program for several different configurations and input parameters. As seen from the graph, increasing the amount of fluid input or steepening the branch angle (131° is steeper than 111°) increases the maximum number of intersections that can be passed by the fluid droplets. This graph can represent a spatial comparison

for different input volumes. The physical depth represented by different fracture inclinations are not the same for different branch angles. Fig. 4.8 is not a comparison of lateral and vertical depth for two β cases, it only represents a comparison of the number of intersections crossed in each case. This is because geometrically, vertical intersections are further spread apart for steeper angles when compared to intersections for shallower angles. Not only does a steeper angle allow for a greater extinction order, as seen in the graph, but the physical depth of the fluid plume is enhanced by the spread out vertical intersections. However, with steeper angles comes intersections that are less spread out horizontally. Steeper fractures may allow for deeper plume depths but shallower fracture angles allow for further lateral fluid movement.

4.6.3 Antisymmetric Fracture Systems

What does the plume front look like for a system of intersections with different aperture widths In nature, orthogonal fracture sets rarely exhibit similar apertures. This asymmetric system is treated similarly to the symmetric case, except that the fracture widths in one direction are allowed to be different than the fracture widths in the other direction. Each droplet coming into each intersection is calculated separately. If either of the interface velocities is negative, the full amount of the incoming droplet, goes into the branch for which $u > 0$, this was discussed in section 4.4.1. For extreme aperture differences, this requirement allows for a "runaway droplet," where a small droplet will continually be rejected

from one fracture aperture and continue on forever down the other aperture always having enough weight to overcome upward capillary forces. This situation is not realistic, as a droplet gets small, it becomes more likely that the fluid will separate into two films instead of remaining a single droplet going down only one side. The films will eventually drain as well.

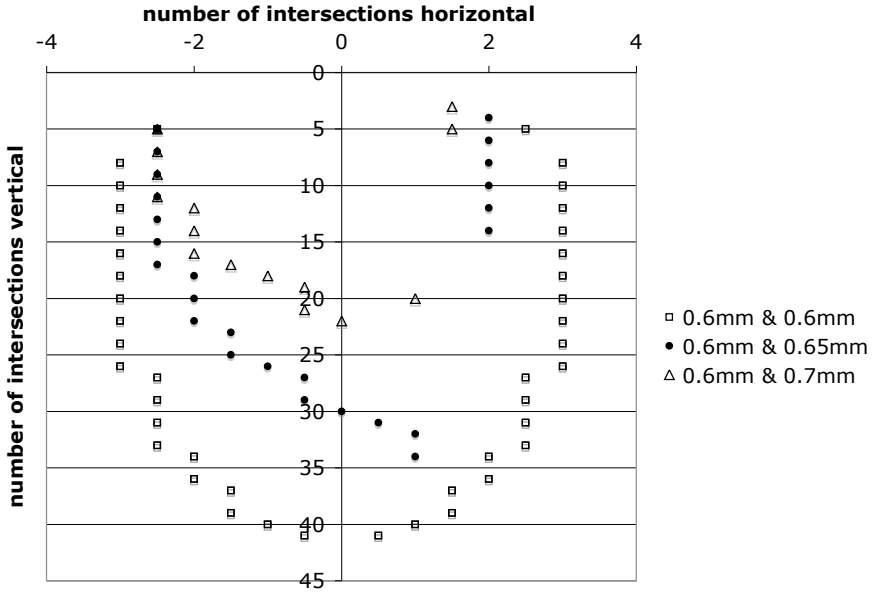

Figure 4.9: Graphed are computer simulated extinction orders in antisymmetric intersection systems for varying differences in the apertures of the branches, specified by the legend (b_1 & b_2).

Fig. 4.9 shows the results of a $10cm$ length droplet inserted into a $0.6mm$

wide fracture ($b_1 = 0.3mm$) and encountering another fracture of greater aperture specified in the graph legend. The system is illustrated in Fig. 4.4 The analysis is dependent on the strengths of gravity and capillarity in each branch. The branch angles are constrained to be equal.

The program used to generate the plots in the previous and current section is included in appendix B.

4.7 Plume Front Discussion

In a network of fractures, as the difference in apertures increases, the maximum extinction order decreases (Fig. 4.9). This is a very important result because it indicates that a symmetric ($b_1 = b_2$) fracture network rather than an antisymmetric one ($b_1 \neq b_2$) maximizes the possible plume front. In natural rock systems, fractures are seldom of equal width and the greater the differences in fracture aperture, the less the fluid will penetrate into the system.

In natural systems, several factors not considered in this analysis could influence the extinction depth. Most of these factors would cause the droplets to penetrate less far, including absorption of the fluid by the rock substrate, evaporation of the fluid, chemical heterogeneities of the rock or fluid that affect contact angle, and mixing of the fluid with others already present in the system. The latter may also contribute to increasing the amount of fluid, increasing the maximum extinction depth. Effectively by ignoring all of these external factors, this study is providing information on the maximum possible plume front.

4.8 Conclusion

A set of intersection rules was derived analytically for a single intersection with variable inclinations and apertures based on fluid properties, fracture geometry, and capillary and gravitational forces. When a droplet encounters an intersection, the fluid is distributed into the available branches according to a competition of forces. The formulas provide a means of comparing the initial strengths of the competing forces on a droplet immediately upon entering the intersection and are given to estimate output droplet volume ratio and eventual terminal velocity of the output droplets. It is also possible for droplets to transition into films at an intersection, however, the flow mode focus here is on droplets, one input droplet becoming two output droplets. Formulas account for the case where a droplet will not enter a branch due to an upward net force into that branch (e.g. a droplet moving from a very narrow fracture to a very wide fracture). This manifests in the equations as a negative fluid-air interface velocity. It was also found that the distribution of liquid into the two branches can be equal even for non-symmetric intersections, and depends on the balance of competing capillary and gravitational forces on the fluid at the onset of the two available branches.

In a system of multiple intersections, the distribution process continues until the weight of the droplets is no longer able to overcome the upward capillary force, then the droplets will not penetrate further into the network. The final placement of droplets is called the maximum plume front. Depth and lateral extent of the plume is maximal for symmetric intersections. Maximum depth attained by fluid

is important for modeling solute transport in rock fracture flow, especially in cases where radioactive liquid contaminant transport moves toward the ground water or pesticide transport in agricultural areas moves toward underground aquifers.

Upscaled simulations give insight into the complex behavior of a fluid plume in fracture networks. The general behaviors discussed are important for understanding possible paths taken by fluid through intersections and the possible maximum depth and lateral extent reached by the fluid. Simulations demonstrate how intersection rules, derived through pore-scale fluid physics may be upscaled to larger models, allowing freedom for changing the fluid properties, geometric parameters and initial conditions. The intersection rules and simulations are based on fundamental physics, not experimental data. In natural rock, other factors will also affect flow and an investigation such as this one should be enhanced to incorporate more intersection branches, different branch angles, fluid absorption into the substrate and transitions into other flow modes such as films or rivulets.

We thank the NSF (Grant 0449928) for financial support.

4.9 References

De Gennes, PG., Hua, X., Levington P., 1990. Dynamics of wetting: Local contact angles. Journal of Fluid Mechanics 212, 55-63.

Dragila, M.I., Weisbrod, N., 2003. Parameters affecting maximum fluid transport in large aperture fractures. Advances in Water Resources, 26: 1219-1228.

Dragila, M.I., Weisbrod, N., 2004. Fluid Motion through an unsaturated fracture junction. Water Resources Research. 40: W02403.

Hoffman, R.L., 1975. A study of the advancing interface I. Interface shape in liquid-gas systems. Journal of Colloid and Interface Science, 50(2): 228-41.

Hoffman, R.L., 1983. A study of the advancing interface II. Theoretical prediction of the dynamic contact angle in liquid-gas systems. Journal of Colloid and Interface Science 94(2): 470-486

Huang, H., Meakin, P., Liu, M., 2005. Computer simulation of twophase fluid motion in unsaturated complex fractures using volume of fluid method. Water Resources Research 41: W12413.

Su, G.W., Geller, J. T., Hunt, J.R., Pruess, K., 2004. Small-scale features of gravity-driven flow in unsaturated fractures. Vadose Zone Journal 3:592-601.

Tartakovsky, A.M., Meakin, P., 2005. Simulation of unsaturated flow in complex fractures using smoothed particle hydrodynamics. Vadose Zone Journal 4:848-855.

Wood, T.R., Nicholl, M.J., Glass, R.J., 2002. Fracture intersections as integrators for saturated flow. Geophysical research letters, 29(24): 2191

Chapter 5 – Summary and Future Work

The first manuscript quantifies the spreading of fluid into a rough surface, implying that the rate of spreading can be predicted, given fluid properties and surface geometry. The theory was constructed around these assumptions: a wetting fluid will invade rough texture, a rough surface allows curved liquid-air interfaces, curved liquid-air interfaces produce capillarity, on small scales capillarity dominates fluid motion and viscous friction in fluid resists forward motion. Driving capillary forces and viscous friction forces are balanced to predict motion of the invasion front.

The theory for fluid spreading on a rough surface was created with a particular surface in mind (Bico et al., 2001), a surface with evenly spaced micron-scale cylindrical pegs in rows. This is not a very realistic simulation of a natural rough surface, namely a rock surface. The predicted motion of the fluid front will have to be reevaluated for random roughness. The current theory made use of a channel approximation for the rough surface, ignoring the effect of flow around each cylinder. Obstructed flow will have to be taken into account for real rough surfaces. The other major change will be to allow for the surface to be porous in addition to rough. As a first approximation, porosity may be seen simply as a loss of fluid per time proportional to the surface area covered in that time. However, the absorption rate will decrease with longer exposure to the substrate. This will decrease the current predicted spreading due to the additional absorption of the wall.

The roughness invasion theory needs to be experimentally tested on real and fabricated rough surfaces that have random roughness, like rock. Experiments of fluid invasion on rock and sand blasted glass plates should include a profile of the rough surface and record the invasion as a function of time. Results should be compared to theoretical formulas for real and fabricated rough surfaces. This project would involve some simple experiments but require very careful recording and analysis since the effect is so small.

The second manuscript describes the need for a complete mathematical description of a moving droplet. The best theoretical speed predictions include properties of the fluid and solid, gravity, capillarity, a dynamic advancing contact angle and a boundary condition changed by roughness (zero degrees original contact angle). This theory cannot adequately explain droplet speed, why? The answer may lie in the internal flow dynamics. Droplet flow should be categorized into regimes of different possible flow behaviors. The different behaviors may point to different mechanisms that slow or enhance droplet speed. It is suggested that the internal flow dynamics be elucidated with florescent colloid movement recorded with a high speed video camera.

As a fluid droplet passes through an intersection the amount of fluid that proceeds into each available brach is governed by the balance of capillary forces (involving width of intersection branches) and gravitational forces (involving branch inclination). Once the pore-scale physics of one intersection is described, it is necessary to upscale to multiple intersections. Experimental and computational simulations illustrate how small scale behavior will control large scale fluid move-

ment in fracture situations. Large scale simulations should allow for differences in fracture apertures and inclinations, as well as transitions between modes of flow (for example the transition of a droplet to a film through an intersection). The model presented in the last manuscript ignores the (larger) curvature of three-dimensional droplets; eventually the three-dimentainality will have to be considered to account for overlapping and sloping fractures.

A full study of intersections should include an investigation of properties of various flow modes. Flow in fractures can take on different forms. In the context of rock fracture contaminant flow, the reason flow mode is important is because different flow modes have different average flow speeds and differing amount of time exposed to the soil/rock matrix.

Understanding the physics of transitions in flow modes will also be important. As an example, a fracture geometry that opens up provides the opportunity for a flow mode transition. For example, the transition between a liquid bridge (droplet) and two separate drops is governed by an instability. The bridge is formed and travels down the fracture until it becomes more favorable for the system configuration to be two separate drops. The instability occurs due to the minimum energy principle, minimum surface energy. The liquid bridge will snap when it becomes energetically favorable to have the surface area of two spherical caps instead of a liquid bridge.

The eventual goal of this project is to understand the physical mechanisms behind fluid movement in fractures and be able to adequately predict this movement. Fluid flow in fractures is immensely complicated, involving fluid dynamics, surface

tension effects, unknown boundary conditions, heterogeneity and varying scales of porosity. Physics is needed to explain idealized variations of the overall problem. This information can be used to improve current flow models in fractured media and thereby begin to unravel the mysteries of contaminant or pesticide flow in dry rocky vadose zones.

Chapter 6 – Bibliography

Bico, J., Marzolin, C., Qué*ré*, D., 1999. Pearl drops. Europhysics Letters 47(2): 220-226.

Bico, J., Qué*ré*, D., 2001. Falling Slugs. Journal of Colloid and Interface Science 243:262-264.

Bico, J., Qué*ré*, D., 2002. Self Propelling Slugs. Journal of Fluid Mechanics. 467:101-127.

Bico, J., Tordeux, C., Qué*ré*, D., 2001. Rough Wetting, Europhysics Letters, 55: 214-220.

Browning, L., Murphy, W.M., Manepallya, C., Fedorsa, R., 2003. Reactive transport model for the ambient unsaturated hydrogeochemical system at Yucca Mountain, Nevada. Computers & Geosciences 29 (3): 247-263.

Burlatsky, S.F., Oshanin, G., Cazabat, A.M., Moreau, M., 1996. Microscopic Model of Upward Creep of an Ultrathin Wetting Film, Physical Review Letters, 76: 86-89.

Butt, H-J., Graf, K., Kappl, M., 2006. Physics and Chemistry of Interfaces. Wiley-Vhc Verlag Gmbh & Co. KGaA, Weinheim

Cassie, A.B.D., Baxter, S., 1944. Wetability of porous surfaces. Transactions of

the Faraday Society Articles 40: 546 - 551

Cazabat, A.M., Cohen Stuart, M.A., 1986. Dynamics of Wetting: Effects of Surface Roughness, Journal of Physical Chemistry, 90: 5845-5849.

De Gennes, P.G., Hua, X., Levinson, P., 1990. Dynamics of wetting: local contact angles. Journal of fluid mechanics 212:55-63.

Dragila, M.I., Weisbrod, N., 2003. Parameters affecting maximum fluid transport in large aperture fractures. Advances in Water Resources 26: 1219-1228.

Dragila, M.I., Weisbrod, N., 2004. Flow menisci corners of capillary rivulets. Vadose Zone Journal 3: 1439-1442.

Dragila, M.I., Weisbrod, N., 2004. Fluid motion through an unsaturated fracture junction. Water Resources Research. 40: W02403.

Dussan, E.B., Davis, S.H., On the motion of a fluid-fluidinterface along a solid surface. Journal of Fluid Mechanics 65(1): 71-95.

Dussan, E.B., Rame, E., Garoff, S., 1991. On identifying the appropriate boundary conditions at a moving contact line: an experimental investigation. Journal of Fluid Mechanics 230:97-116.

Fairley, J.P., Podgorney, R.K., Wood, T.R., 2004. Unsaturated flow through a small fracture-matrix network: Part 1. Uncertainty in modeling flow processes. Vadose Zone Journal 3:101-108.

Glass, R.J., Nicholl, M.J., Pringle, S.E., Wood, T.R., 2002. Unsaturated flow

through a fracture-matrix network: Dynamic preferential pathways in mesoscale laboratory experiments. Water Resources Research 38(12): 1281-1298.

Hoffman, R.L., 1974. A study of the advancing interface I. Interface shape in liquid-gas systems. Journal of Colloid and Interface Science 50(2): 228-241.

Hoffman, R.L., 1983. A study of the advancing interface I. Theoretical prediction of the dynamic contact angle in liquid-gas systems. Journal of Colloid and Interface Science 94(2): 470-486.

Huang, H., Meakin, P., Liu, M., 2005. Computer simulation of twophase fluid motion in unsaturated complex fractures using volume of fluid method. Water Resources Research 41: W12413.

Huh, C., Mason, S.G., 1977. The steady movement of a liquid meniscus in a capillary tube. Journal of Fluid Mechanics 81(3): 401-419.

Nieminen, J.A., Abraham, D.B., Karttunen, M., Kashi, K., 1992. Molecular dynamics of a microscopic droplet on solid surface. Physical Review Letters 69(1): 124-127.

Nimmo, J.R., 2007. Simple predictions of maximum transport rate in unsaturated soil and rock. Water Resources Research. 43, W05426.

Nunn, R.H., 1989. Fluid Mechanics. Hemisphere Publishing Corporation, New York.

Pruess, K., Yabusakib, S., Steefelc, C., Lichtnerd, P., 2002. Fluid Flow, Heat

Transfer, and Solute Transport at Nuclear Waste Storage Tanks in the Hanford Vadose Zone. Vadose Zone Journal, 1:68-88

Qu*é*r*é*, D., 2002. Rough Ideas on Wetting. Physica A., 313: 32-46.

Shah, R.K., A. L. London, A.L., 1978. Advances in Heat Transfer, Academic Press, New York.

Steele, B., 2004. A Comparison of Theoretical and Experimental Capillary Droplet Speeds on Porous and Non-Porous Fracture Surfaces. Master of Environmental Soil Science Thesis, Oregon State University, Corvallis, Oregon.

Su, G.W., 1999. Flow Dynamics and Solute in Unsaturated Rock Fractures. PhD Thesis, University of California Berkley, Department of Civil and Environmental Engineering and Ernest Orlando Lawrence Berkley National Laboratory, Earth Sciences Division.

Su, G.W., Geller, J. T., Hunt, J.R., Pruess, K., 2004. Small-scale features of gravity-driven flow in unsaturated fractures. Vadose Zone Journal 3:592-601.

Su, G.W., Geller, J.T., Pruess, K., Hunt, J.R., 2001. Solute transport along preferential paths in unsaturated fractures. Water Rsources Research 37(10): 2481-2491.

Su, G.W., Nimmo, J.R., Dragila, M.I., 2003. Effect of isolated fractures on accelerated flow in unsaturated porous rock. Water Resources Research 39(12):1326-1335.

Tartakovsky, A.M., Meakin, P., 2005. Simulation of unsaturated flow in complex fractures using smoothed particle hydrodynamics. Vadose Zone Journal 4:848-855.

Thompson, P.A., Robbins, M.O., 1989. Simulations of contact line motion:slip and the dynamic contact angle. Physical Review Letters 63(7): 766-769.

Washburn, E.W., 1921. The Dynamics of Capillary Flow, Physical Review 17: 273-283.

Wenzel, R.N., 1936. Resistance of Solid Surfaces to Wetting by Water. Industrial Engineering Chemistry, 28: 988-994.

White, F.M., 1991. Viscous Fluid Flows, McGraw-Hill, Boston.

Wood, T.R., Glass, R.J., McJunkin, T.R., Podgorney, R.K., Laviolette, R.A., Noah, K.S., Stoner, D.L., Starr, R.C., Baker, K., 2004. Unsaturated flow through a small fracture-matrix network: Part 1. Experimental Observations. Vadose Zone Journal 3:90-100.

Wood, T.R., Nicholl, M.J., Glass, R.J., 2002. Fracture intersections as integrators for saturated flow. Geophysical research letters, 29(24): 2191

APPENDICES

Appendix A – Extinction order of plume edge program (java)

```
//
//  Extinction_Order.java
//  Extinction_Order
//
//  Created by Katrina Hay on 2/25/08.
//  Copyright (c) 2008 __Oregon State University__. All rights reserved.
//

import java.util.*;
import java.lang.Math.*;
import java.io.*;

public class Extinction_Order {
// This program allows a droplet to progress through a number of
//symetric three-way intersections,
// to determin how many intersections (orders) can be passed
//before the droplet is
// too small to continue (extinction order).
// The purpose is to study the affect of intersection angle on
```

```
//extinction order.

public static void main (String args[]) throws IOException {

//All variables are in SI units
int order = 0; // number of intersections passed
double PI = 3.14159;

//Geometric parameters of the problem:
double initial_length = 0.1;
// length of droplet before first intersection
double advancing_contact_angle = 15 *PI/180;
// 15 degrees, Advancing contact angle, could later be made dynamic.
// Receding contact angle is assumed zero.

//Fluid properties and accelleration due to gravity:
double viscosity = 1.002*Math.pow(10,-3);
double density = 1000.0;
double surface_tension = 0.072;
double gravity = 9.8;

//Variables in problem:
double width = .001; // width of all intersection branches
```

```
// Asks you to give a width before running the program:
BufferedReader SystemIn = new BufferedReader(
new InputStreamReader(System.in)  );
System.out.print("Intersection branch width (in meters): ");
width = Double.parseDouble(SystemIn.readLine());

double percentage = .5; // defines percentage of droplet that
//progresses to next branch (between 0 and 1)
// Asks you to give a percentage before running the program:
// BufferedReader SystemIn = new BufferedReader(
// new InputStreamReader(System.in)  );
// System.out.print("Percentage of length to progress to
//next branch (between 0 and 1): ");
// percentage = Double.parseDouble(SystemIn.readLine());

double angle = 101.0*PI/180.0;
// starting angle intersection branches exit from vertical
//(90 degrees to 180 degrees)


try{
// Create file for extinction order vs. branch angle:
FileWriter fstream2 = new FileWriter("extorder_vs_angle" +width+".txt");
```

```
BufferedWriter extorder_out = new BufferedWriter(fstream2);


//This loop runs a droplet through a system of intersections
//for different angles from 90-180 degrees.
//The angles change by the factor in this added term:
//(currently 5 degrees)
for( ; angle < PI; angle = angle +(5*PI/180))
{

// Create file for how the fluid speed changes as it travels
//through one system
FileWriter fstream = new FileWriter("order_vs_vel" +
Math.floor(angle*180/PI) + width+".txt");
BufferedWriter out = new BufferedWriter(fstream);

double length = initial_length; //input initial droplet length
System.out.println("\nbranch exit angle =" +angle*(180/PI));
// "\n" adds a return before next line
double minimum_length = (surface_tension/(density*gravity*
Math.cos(PI-angle)))*((1/width)-(Math.cos(advancing_contact_angle)
/width));
//This minimum length defines when the droplet is nolonger large
```

```
//enough to continue to move down.

System.out.println("minimum length =" +minimum_length);
//prints minimum length condition to the screen.


//This loop progresses the droplet through intersections
// (orders) until it can no longer move down.
//The velocity of the new droplet is found after each intersection,
//the last order is the "extinction order"
for(order=0; length > minimum_length; order++)
{
double terminal_velocity = (((width*width)/(3 * viscosity))*
((density*gravity*Math.cos(PI-angle))
+ ((surface_tension/length)*((Math.cos(advancing_contact_angle)/width)
-(1/width)))));


System.out.println("terminal velocity = " + terminal_velocity +"  "
+ "order=" +order);
// Write data to file
out.write(order + ", " + terminal_velocity +"\n");
length=length*percentage;
```

```
}//ends order length loop
System.out.println("terminal velocity = " + 0 +"  "+ "order="
+(order));
out.write((order) + ", " + 0 +"\n");

extorder_out.write(order + ", " + +angle*(180/PI) +"\n");
//Prints the extinction order (number of intersections passed total,
// associated with minimum length) and specific angle.

//Close the output stream to file for the order vs. velocity data
out.close();

}// angle loop bracket

//Close the output stream to file for the extinction order vs.
//angle data
extorder_out.close();

}catch (Exception e){//Catch exception if any for file creation
System.err.println("Error: " + e.getMessage());
}// catch bracket for second created file
```

```
}//ends public static void

}//ends public class
```

Appendix B – Antisymmetric maximum plume front program (java)

```
//
//  Antisymetric_plume_front.java
//  Antisymetric_plume_front
//
//  Created by Katrina Hay on 3/6/08, template for program by Zachary Wiren.
//  Copyright (c) 2008 __Oregon State University__. All rights reserved.
//
import java.util.*;

public class Antisymetric_plume_front {
//This program calcultaes the maximum plume front for droplets
//falling a down a system of antisymetric (different widths) intersections
//the output is a positional plot of last intersections
//downward passed by fluid droplets
//fluid parameters can be chaged as well as intersection widths
//and initial fluid amount.
//A file is created that lists the extinction positions of the last
//fluid droplets.
//Has a problem with runaway droplets, when one interface has
```

```
//a negative velocity.

public static void main (String args[]) {



//All variables are in SI units
int order = 0; //number of intersections passed (vertically)
double PI = 3.14159;

//Fluid properties and accelleration due to gravity:
double viscosity = 1.002*Math.pow(10,-3);
double density = 1000.0;
double surface_tension = 0.072;
double gravity = 9.8;

//Geometric parameters of the problem, can change these:
double initial_length = 0.1;
// 10 cm, length of droplet before first intersection
double advancing_contact_angle = 15 *PI/180;
// 15 degrees, Advancing contact angle,
// could later be made dynamic
// Receding contact angle is assumed zero
```

```
//Variables in problem, can change these,
//they can be different (antisymetric):
double width1 = .0003;
// width (in meters) of left-going intersection branches
double width2 = .0004;
// width of right-going intersection branches

//set to zero: fluid-air interface velocity,
//then volume ratio (1 to 2)
double interface_speed1 = 0.0;
double interface_speed2 = 0.0;
double volume_ratio = 0.0;
double total_volume = 0.0;


// due to geometrical complications in counting orders,
//these angles have to be the same for now:
double angle1 = 120.0*PI/180.0;
// starting angle left-going intersection branches
//exit from vertical
//(90 degrees to 180 degrees)
double angle2 = 120.0*PI/180.0;
// starting angle right-going intersection branches
```

```
//exit from vertical
//(90 degrees to 180 degrees)


//mimumum length that will be supported
//in this system (capillarity over comes gravity):
double minimum_length1 = (surface_tension/(density*gravity
*Math.cos(PI-angle1)))*((1/width1)-
(Math.cos(advancing_contact_angle)/width1));
System.out.println("minimum length, 1 =" +minimum_length1);
//prints left-going minimum length condition to the screen.
double minimum_length2 = (surface_tension/(density*gravity
*Math.cos(PI-angle2)))*((1/width2)-
(Math.cos(advancing_contact_angle)/width2));
System.out.println("minimum length, 2 =" +minimum_length2);
//prints right-going minimum length condition to the screen.


//Defines array to store the length
//(amount of fluid coming into each intersection)
int max_width = 300; //max number of j's
//(intersections across) allowed, avoid overcomputation
double[] length1 = new double[ max_width] ;
```

```
//define array for current level
double[] length_one_order_lower1 = new double[max_width + 1];
// Define array for next level

double[] length2 = new double[ max_width] ;
//define array for current level
double[] length_one_order_lower2 = new double[max_width + 1];
// Define array for next level

//to be computed for each intersection,
//once for left incoming, once for right incoming:
double split_length1 = 0.0;
//length of remaining left-going droplet ater intersection
double split_length2 = 0.0;
//length of remaining right-going droplet after intersection


for(order = 0; order < max_width; order++){
// orders are vertical levels of intersections
length1[order] = 0.0;
length_one_order_lower1[order] = 0.0;
//set all array values equal to zero
length2[order] = 0.0;
```

```
length_one_order_lower2[order] = 0.0;
//set all array values equal to zero
}
length_one_order_lower1[max_width] = 0.0;
//set max array value equal to zero
length_one_order_lower2[max_width] = 0.0;
//set max array value equal to zero

// liquid flowing into the intersection system (100%)
//always start with fluid coming into the first intersection
//through the width1 branch
length1[0] = initial_length;
length2[0] = 0.0;

// loop for how deep into the layers (orders):
// not allowed to go any deeper than max_width to avoid writting
// outside the array
//here begins the process of fluid moving through intersections:
for( order = 0; order < max_width; order++ ){

// loop for how far across the layers:
for(int j = 0; j <= order; j++){
// if there is fluid coming into the
```

```
//intersection divide it in half or other percentage,
//if the droplet is too small output the position
//of the intersection to plot

//Computes fluid movement for width1 incoming
//droplets on each order
if( length1[j] > minimum_length1/1000.0 )
{
if(length1[j] < minimum_length1)
{

// prints out the last intersections that the droplets
//travel through before they are too small to fall
//record x and y position of stop, zero is under droplet entry
System.out.println( (j-1) - ((order-1)/2.0) + ", " + (order-1) );
//double counts points for symetric case

// prints out last place the droplets will be found stopped before
//next intersection
//the above printout gives a smoother graph than this one:
//System.out.println( j - ((order+1.0)/2.0) + ", " + (order+1) );
//System.out.println( (j+1) - ((order+1.0)/2.0) + ", " + (order+1) );
```

```
}
else
{

//System.out.println( order + ", " +length1[j] + "\n" );
//records lengths to check
//calculate fluid-air interface velocity, then volume ratio (1 to 2)
//calculating interface speed: incoming width matters and original
//length is different depending on width
interface_speed1 = ((width1*width1)/3*viscosity)
*((density*gravity*Math.cos(PI-angle1))+
((surface_tension/length1[j])*((Math.cos(advancing_contact_angle)/width1)
-(1/width1))));

interface_speed2 = ((width2*width2)/3*viscosity)*
((density*gravity*Math.cos(PI-angle2))+
((surface_tension/length1[j])*((Math.cos(advancing_contact_angle)/width2)
-(1/width1))));
volume_ratio = (interface_speed1*width1)/(interface_speed2*width2);

//if(j==order/2) System.out.println(  "Order: " + order + ",
//Vol Ratio1: " + volume_ratio  );
//checks vol ratio
```

```
split_length1 = (length1[j]*width1)/(width1*(1+(1/volume_ratio)));
//split length when it passes intersection
split_length2 = (length1[j]*width1)/(width2*(1+(volume_ratio)));
//split length when it passes intersection

// If one of the speeds is negative, give all fluid to other branch:
if(interface_speed1 < 0.0)
{
split_length1 = 0.0;
split_length2 = width1*length1[j]/width2;
}
if(interface_speed2 < 0.0)
{
split_length2 = 0.0;
split_length1 = width1*length1[j]/width1;
}
//System.out.println( order + "First: splitlength1= " + split_length1
//+ "splitlength2= " + split_length2  );

//Adds up fluid to the next intersection array element going each way
length_one_order_lower1[j+1] = length_one_order_lower1[j+1] + split_length1;
length_one_order_lower2[j] = length_one_order_lower2[j] + split_length2;
```

```
}

}

//Computes fluid movement for width2 incoming droplets on each order
if( length2[j] > minimum_length2/100.0 )
{
if(length2[j] < minimum_length2)
{

// prints out the last intersections that the droplets
//travel through before they are too small to fall
//record x and y position of stop, zero is under droplet entry
System.out.println( (j) - ((order-1)/2.0) + ", " + (order-1) );
//double counts points for symetric case

// prints out last place the droplets will be found stopped before
//next intersection
//the above printout gives a smoother graph than this one:
//System.out.println( j - ((order+1.0)/2.0) + ", " + (order+1) );
//System.out.println( (j+1) - ((order+1.0)/2.0) + ", " + (order+1) );

}
```

```
else
{

//calculate fluid-air interface velocity, then volume ratio (1 to 2)
//calculating interface speed: incoming width matters and original
//length is different depending on width
interface_speed1 = ((width1*width1)/(3*viscosity))*
((density*gravity*Math.cos(PI-angle1))+((surface_tension/length2[j])*
((Math.cos(advancing_contact_angle)/width1)-(1/width2))));

interface_speed2 = ((width2*width2)/(3*viscosity))*
((density*gravity*Math.cos(PI-angle2))+((surface_tension/length2[j])*
((Math.cos(advancing_contact_angle)/width2)-(1/width2))));

volume_ratio = (interface_speed1*width1)/(interface_speed2*width2);

// if(interface_speed1 < 0.0) //checks to see which speeds are negative,
//affect on vol ratio
// {
// System.out.println( "Order: " + order + ", Vol Ratio2: "
//+ volume_ratio);
// System.out.println( "\t interface_speed1: " + interface_speed1);
// System.out.println( "\t interface_speed2: " + interface_speed2);
```

```
// }


split_length1 = (length2[j]*width2)/(width1*(1+(1/volume_ratio)));
//split length when it passes intersection
split_length2 = (length2[j]*width2)/(width2*(1+(volume_ratio)));
//split length when it passes intersection

// If one of the speeds is negative, give all fluid to other branch:
if(interface_speed1 < 0.0)
{
split_length1 = 0.0;
split_length2 = width2*length2[j]/width2;
}
if(interface_speed2 < 0.0)
{
split_length2 = 0.0;
split_length1 = width2*length2[j]/width1;
}

length_one_order_lower1[j+1] = length_one_order_lower1[j+1] + split_length1;
```

```
length_one_order_lower2[j] = length_one_order_lower2[j] + split_length2;
}

}

} // End loop across each order, j's

// transfer from length_one_order_lower to length,
//and zero out length_one_order_lower
for(int j=0; j<max_width; j++){
length1[j] = length_one_order_lower1[j];
length_one_order_lower1[j] = 0.0;
total_volume = total_volume + length1[j]*width1;

length2[j] = length_one_order_lower2[j];
length_one_order_lower2[j] = 0.0;
total_volume = total_volume + length2[j]*width2;
}

// System.out.println( "Order: " + order + ", Volume Remaining: "
//+total_volume ); //program check point
total_volume = 0.0;
length1[0] =0.0;
```

```
length_one_order_lower1[max_width]=0.0;

length_one_order_lower2[max_width]=0.0;

} // End loop through orders (depth of intersections)



} //ends public static void main

} //ends public class
```